· U C ·

# Modeling the Magnetic Field of Mercury

by Joana Oliveira

Master Thesis in Astrophysics and Space Instrumentation

Supervisors:
Dr. M. Alexandra Pais
Dr. Benoit Langlais

Universidade de Coimbra
July, 2011


Universidade de Coimbra

# Modeling the Magnetic Field of Mercury

Master Thesis in Astrophysics and Space Instrumentation

by Joana Oliveira

Supervisors
Dr. M. Alexandra Pais
Dr. Benoit Langlais

July 20, 2011

## Acknowledgements

I am thankful to a lot of persons that supported me in different ways while I was developing my work, as a scientist and as a person. Thanks to:

A perfect combination of supervisors, Benoit Langlais and Alexandra Pais (the Yin Yang supervisors) who have contributed very positively and helped me to overcome the difficulties during my thesis work!

Ao Gafeira e Carina, estiveram, estão e estarão sempre quando preciso dum ombro amigo.

Ao Professor Peixinho, obrigada por me ter dito como numerar as páginas em romano!

Às senhoras da biblioteca... as preciosas conversas de longos quartos de hora, que ajudaram a desanuviar!

Solmaz et Marine, les amies de Nantes! Merci pour votre amitié.

**Abstract**

In this thesis work I have been concerned with modeling the magnetic field of planet Mercury. With this goal in mind, I tested a new method for modeling the time dependent magnetic field of a planet, the Time Variable Equivalent Source Dipole method. I showed that in the case that applies to Mercury, namely a concentration of observations over the northern hemisphere, this method gives better results than the standard Spherical Harmonic method.

The main conclusion of this thesis is that, assuming that the secular variation of Mercury is around one tenth of its main field, in amplitude, the new developed method will allow to recover it from MESSENGER data. This has very important consequences for the understanding of the core dynamics and in particular of the dynamo mechanism that generates Mercury magnetic field.

This work is finished, but the problem is not solved. Nevertheless, it clarified different questions that will make it easier to continue for the analysis of the true measures of MESSENGER spacecraft.

# Contents

# List of Figures

# Chapter 1

# The Planet Mercury

The planet Mercury is one of the most peculiar of the solar system. It is the smallest of the telluric planets, with a metal density higher than the others. The intense craterization suggests that it was one of the first telluric planets to stop its geological activity. Moreover, it is the closest planet to the Sun, and because of that it has the largest range in diurnal temperatures. It is the only one that is locked to a spin-orbit resonance (3:2), and its atmosphere is the most tenuous among the terrestrial planets[1]. Table 1.1 shows values for the most important astronomical parameters for Mercury. But its most important characteristic concerning this thesis, is the fact that it has a global magnetic field, probably of internal origin!

In this chapter, I will talk particularly about some issues that are relevant to the thesis subject.

## 1.1 Internal structure of Mercury

The formation of the planet is not yet well understood. It is believed that the structure of Mercury consists in crust, mantle, and core. Figure 1.1 shows the internal structure thought to be the hermean one. There still exists an uncertainty on the sizes of each constituent. From gravimetry and astronomical measurements of the mass and rotation of Mercury, the core radius size is in a range $[1800\ km, 2200\ km]$. The crust thickness has been also evaluated to be around 100 $km$, from geodetic measurements [3].

The chemical composition of the planet is also unknown. Experimental works as [3], show different formation scenarios characterized by different geochemical models, using very different oxide/silicate ratios, and try to understand which composition

Table 1.1: Gravimetric and astronomical parameters for Mercury [2].

| Characteristics | |
|---|---|
| Sidereal Orbital Period | 87.969 *day* |
| Average orbital speed | 47.873 $km/s$ |
| Orbital Inclination | 7.005° (to Ecliptic) |
| Aphelion | 0.467 *AU* |
| Perihelion | 0.307 *AU* |
| Semi-major axis | 0.387 *AU* |
| Eccentricity | 0.206 |
| Mean radius | 2440 $km$ |
| Volume | $6.083 \times 10^{10}$ $km^3$ |
| Mass | $3.302 \times 10^{23}$ $kg$ |
| Mean density | 5.427 $g/cm$ |
| Equatorial gravity | 3.7 $m/s^2$ |
| Escape velocity | 4.435 $km/s$ |
| Sidereal rotation period | 58.646 *day* |
| Obliquity to orbit | $2.11'$ |

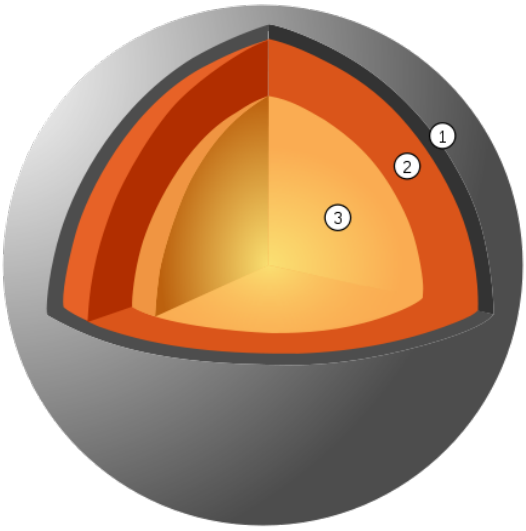


Figure 1.1: Mercury internal structure: 1 - crust; 2 - mantle; 3 - core. by Joel Holdsworth.

fits better what we already know about the planet.

It is Mercury's core, the constituent most important to this thesis. Concerning the physical state of Mercury's core, there is an indication that the mantle of Mercury is decoupled from a core that is partially molten [4]. This results from interpretation of radar measures together with the Mariner 10 determination of the gravitational harmonic coefficients. Moreover, in [5] is suggested that Mercury's core may have a complex shell structure comprising an outer core layer of liquid Fe-S and poor in Si, a middle layer of liquid Fe-Si poor in S, and an inner core of solid metal. Furthermore, they think that it could be the heat from the decay of uranium to act to maintain the outer core's layer molten, a result that contrasts with the Earth's case (where the radioactive decay of uranium is a negligible contribution to core heating).

## 1.2 Magnetic Field and Magnetosphere

Because of the relatively large external magnetic field due to magnetopause and magnetotail currents, large temporal field fluctuations, and a relatively small magnetospheric cavity, the separation between internal and external contributions becomes particularly difficult. It was with Mariner 10, that the speculation that the observed

magnetic field might be due to a solar wind induction was forsaken. A maximum field intensity of 400 $nT$ was measured then. With a clear identification of the global magnetic field as being due to an internal source, the possibilities for the kind of source are an active dynamo or a remanent magnetic field (due to permanently magnetized minerals, at sub-Curie point temperatures). There is still some doubt to choose between these sources, because it is impossible to distinguish the contributions from an active dynamo or remanent magnetization in one single epoch, even with a perfect description of the global magnetic field [6]. Supplementary information on the magnetic field time variation (secular variation) is essential for this discrimination. In [7] the author shows that the weak magnetic field measured can have origin in a magnetized non-uniform shell, using the Runcorn's theorem [8]. During the first flyby, MESSENGER has measured data that shows that the planetary field is mainly and possibly entirely dipolar [9].

# Chapter 2

# The mission MESSENGER

The difficulty to observe the first planet of the solar system from the Earth was a strong motivation to pursue space missions that target Mercury.

The first spacecraft that has visited Mercury was Mariner 10, in the 1970s. This spacecraft carried a magnetometer, a situation that in the end was very fortunate since, contrary to what was previously thought, Mercury possessed an internal magnetic field. After that, many missions were proposed, but unfortunately they were not realized. In the late 1990s, two missions were agreed - MESSENGER, carried by the american agency *National Aeronautics and Space Administration*, NASA, and BepiColombo carried by the *European Space Agency*, ESA, and by *Japan Aerospace Exploration Agency*, JAXA [10]. MESSENGER spacecraft is already collecting new Mercury's data (it's orbital insertion was at March 18, 2011), and BepiColombo will be launched in 2014 (it's orbital insertion will take place during 2020).

The spacecraft MESSENGER (MErcury Surface, Space ENvironment, GEochemistry, and Ranging) is three-axis stabilized and carries a variety of instruments for planetary and magnetospheric studies. The three-axis stabilization is a method used to maintain the spacecraft in the desired orientation. With this method, the solar panels can be kept facing the Sun, a directional antenna can be kept pointed at Earth, and cameras can be kept pointed to Mercury's surface.

In the next sections I will summarize the design of this mission, and describe the instruments that MESSENGER is carrying.

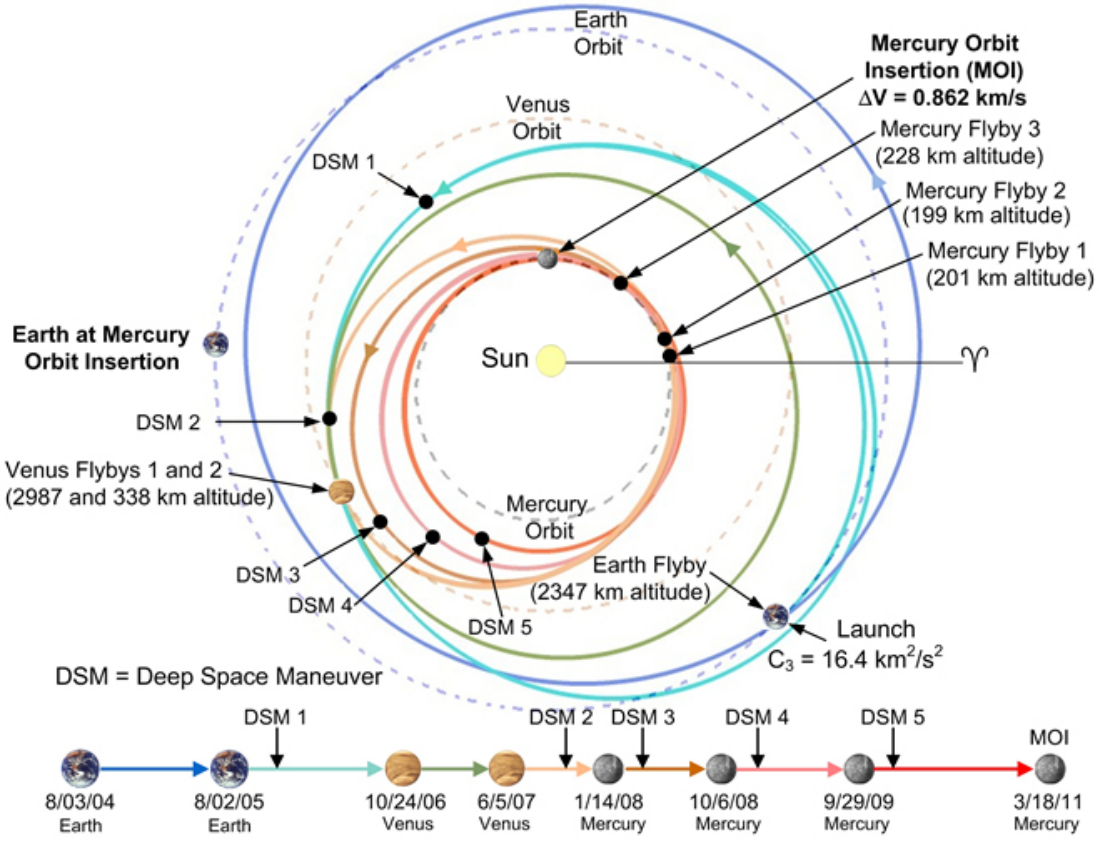


Figure 2.1: Overview of MESSENGER travel. The journey started at launch, did a couple of flybys to Earth, Venus and Mercury, and finally the insertion occurred at the MOI point [11].

## 2.1 Mission Design

To arrive to Mercury, MESSENGER followed a long journey through the inner solar system. Figure 2.1 shows the itinerary, since it's launch to the Mercury orbital insertion (MOI) point. The mission began with launch on August 3, 2004. After almost one year, on August 2, 2005, it returned to Earth for a gravity assist maneuver. Then, MESSENGER continued in direction to Venus, where it did two flybys (on October 24, 2006, and on June 5, 2007). The Mercury flybys occurred on January 14, 2008, on October 6, 2008, and on September 29, 2009, and consisted in the first spacecraft approximation to this planet after 30 years. During the travel, MESSENGER performed many maneuvers to adjust its path to Mercury.

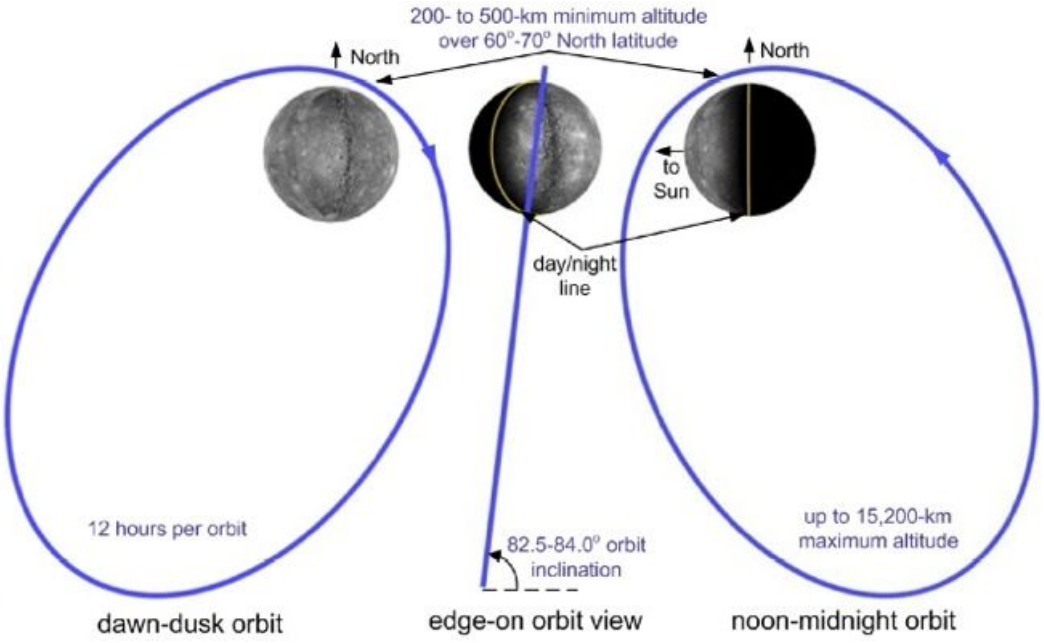


Figure 2.2: The operational orbit of MESSENGER [11].

During the three Mercury flybys, the spacecraft collected new data of the planet, taking pictures of the regions not seen by Mariner 10, the first spacecraft to visit Mercury. The new data allowed to plan strategies for MESSENGER's historic yearlong orbit mission.

After MOI, MESSENGER entered at it's operational orbit represented in figure 2.2. The orbit has a minimum altitude of 200 $km$ at periapsis, between $[60°, 70°]$ North latitude, and a maximum altitude of 15.200 $km$ at apoapsis. The orbit has a time period of 12 hours, and an inclination around $[82.5°, 84°]$.

## 2.2 Instruments

It is a balance between answering as many science questions as possible and the availability of resources, mass, power, mechanical accommodation, and cost, that assist us in choosing the instruments that the spacecraft carries with.

Figure 2.3 shows an overview of the instruments that MESSENGER carries. The Mercury Dual Imaging System (MDIS), is a multi-spectral system, that has wide- and narrow-angle cameras, both based on charge-coupled devices (CCDs). They were constructed to map the rugged landforms and spectral variations on Mercury's surface in monochrome, color, and stereo. The imager pivots, give it the ability to

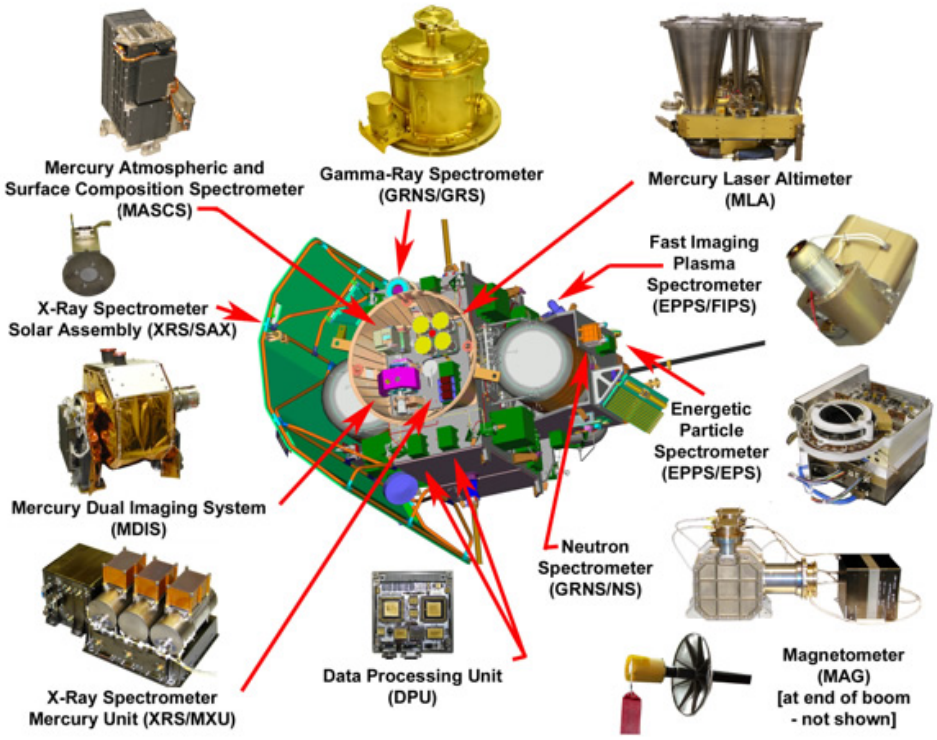


Figure 2.3: Overview of MESSENGER's instruments [11].

capture images from a large area without having to re-point the spacecraft and allow it to follow the stars and other optical navigation guides. The multi-spectral imaging will help scientists investigate the diversity of rock types of Mercury's surface.

The Gamma-Ray and Neutron Spectrometer (GRNS) consist in a gamma-ray and a neutron spectrometers (GRS and NS, respectively), to collect complementary data on elements of Mercury's crust. GRS measures gamma rays emitted by the nuclei of atoms on Mercury's surface that are struck by cosmic rays, and NS maps variations in the fast, thermal, and epithermal neutrons Mercury's surface emits, when struck by cosmic rays. The X-Ray Spectrometer (XRS) maps the elements in the top millimeter of Mercury's crust using three gas-filled detectors (Mercury X-Ray Unit) pointing at the planet, one silicon solid-state detector pointing at the Sun (Solar Assembly for X-rays), and the associated electronics (Main Electronics for X-rays). The planet-pointing detectors measure fluorescence, the X-ray emissions coming from Mercury's surface after solar X-rays hit the planet. The Sun-pointing detector measures the X-rays that are bombarding the planet, coming from the Sun.

The Magnetometer (MAG) is a three-axis, ring-core fluxgate detector. MAG will measure the magnetic field of the planet in detail, helping scientists to determine the field's magnitude and how it varies with position. Obtaining this information is a critical step to search for Mercury's internal magnetic field. Moreover, this sensor is mounted on a 3.6 meters boom that keeps it away from the spacecraft's own magnetic field. To protect it from the Sun, the sensor has also its own sunshade, because it is far from the main spacecraft's body that is also protected from the sun. The instrument will collect magnetic field data with different intervals, that is, 50 milliseconds interval when the spacecraft is near Mercury's magnetosphere boundaries, and one-second interval in the rest of the orbit.

The Mercury Laser Altimeter (MLA) maps Mercury's landforms and other surface characteristics using an infrared laser transmitter and a receiver that measures the round-trip time of individual laser pulses. This data will be also used to get the planet's slight, forced libration, which will tell us about the state of Mercury's core. Moreover, the MLA data combined with Radio Science Doppler ranging will be used to map the planets gravitational field.

Mercury Atmospheric and Surface Composition Spectrometer (MASCS), combining an ultraviolet spectrometer and infrared spectrograph, will measure the abundance of atmospheric gases around Mercury and detect minerals in its surface materials.

The Ultraviolet and Visible Spectrometer (UVVS) will determine the composition and structure of Mercury's exosphere and study it's neutral gas emissions. It will also search for and measure ionized atmospheric species. Together, these measurements will help us understand the processes that generate and maintain the atmosphere, the connection between surface and atmospheric composition, the dynamics of volatile materials on and near Mercury, and the nature of the radar-reflective materials near the planets poles.

The Energetic Particle and Plasma Spectrometer (EPPS) measures the mix and characteristics of charged particles in and around Mercury's magnetosphere using an Energetic Particle Spectrometer (EPS), that observes ions and electrons accelerated in the magnetosphere, and a Fast Imaging Plasma Spectrometer (FIPS).

Finally, the Radio Science (RS) observations measure the MESSENGER's speed and distance from Earth. From this information, we can watch changes in MESSENGER's movements around Mercury to measure the planet's gravity field, and to support the laser altimeter investigation to determine the size and condition of Mercury's core [11].

# Chapter 3

# Mathematical tools for modeling the magnetic field

In this chapter I will present two mathematical models that can describe the magnetic field in a region outside current sources. I will also introduce some algebraic tools that are used for modeling an observed field.

The magnetic field **B** verifies the Maxwell equations below,

$$\nabla \times \mathbf{B} = \mu_0 \mathbf{J} \tag{3.1}$$

$$\nabla \cdot \mathbf{B} = 0 \tag{3.2}$$

Where **J** is the current density and $\mu_0$ is the permeability for free space. From equation 3.1 we can say that **B** is a scalar potential gradient, when we are in a region without sources, i. e. $\mathbf{J} = 0$. Then,

$$\mathbf{B} = -\nabla V \tag{3.3}$$

and from equation 3.2 we obtain the Laplace equation, for the scalar potential V:

$$\nabla^2 V = 0 \tag{3.4}$$

## 3.1 Spherical harmonic (SH) model

In spherical coordinates $(r, \theta, \phi)$, this equation takes the form,

$$\frac{1}{r}\frac{\partial^2(rV)}{\partial r^2}+\frac{1}{r^2\sin\theta}\frac{\partial}{\partial\theta}\left(\sin\theta\frac{\partial V}{\partial\theta}\right)+\frac{1}{r^2\sin^2\theta}\frac{\partial^2 V}{\partial\phi^2}=0 \tag{3.5}$$

Gauss showed that the solution of this equation can be written in the form of spherical harmonics of the potential. That is,

$$V_{n,m}\left(r,\theta,\phi\right)=\left[A_n r^n+B_n r^{-(n+1)}\right]\left[a_m\cos m\phi+b_m\sin m\phi\right]P_{n,m}\left(\cos\theta\right) \tag{3.6}$$

where $P_{n,m}$ are the associate Legendre functions and n, m are integers.

$$P_{n,m}(\mu)=\left(1-\mu^2\right)^{\frac{m}{2}}\frac{d^m P_n(\mu)}{d\mu^m} \tag{3.7}$$

whith $\mu=\cos\theta$, where $P_n(\mu)$ are the Legendre polynomials.

The general solution for Laplace's equation, 3.6, can then be written,

$$V\left(r,\theta,\phi\right)=a\sum_{n=1}^{\infty}\sum_{m=0}^{n}\{\left(g_n^m\cos m\phi+h_n^m\sin m\phi\right)\left(\frac{a}{r}\right)^{n+1}+ \\ +\left(q_n^m\cos m\phi+s_n^m\sin m\phi\right)\left(\frac{r}{a}\right)^{n}\}P_n^m(\theta) \tag{3.8}$$

The equation 3.8 is the potential expansion in spherical harmonics, with $a$ the surface of reference, and $r$ the surface where we want to obtain the potential.

The functions $P_n^m(\theta)\cos m\phi$ and $P_n^m(\theta)\sin m\phi$ are the spherical harmonics, and $g_n^m$, $h_n^m$, $q_n^m$ e $s_n^m$ are the spherical harmonic coefficients.

Studying equation 3.8, the term $\left(\frac{a}{r}\right)^{n+1}$ is zero when r is going to infinity, meaning that this parcel describes the potential of internal sources at the surface reference ($r=a$), usually the Earth's surface. On the other hand the term $\left(\frac{r}{a}\right)^{n}$ is zero when r is going to zero, and that means that this parcel describes the external sources.

Finaly, using the equation 3.3, we obtain the three magnetic field components below,

$$B_r=\sum_{n=1}^{\infty}\sum_{m=0}^{n}\{(n+1)\left[g_n^m\cos m\phi+h_n^m\sin m\phi\right]\left(\frac{a}{r}\right)^{n+2}- \\ -n\left[q_n^m\cos m\phi+s_n^m\sin m\phi\right]\left(\frac{r}{a}\right)^{n-1}\}P_n^m(\theta) \tag{3.9}$$

$$B_\theta=-\sum_{n=1}^{\infty}\sum_{m=0}^{n}\{\left[g_n^m\cos m\phi+h_n^m\sin m\phi\right]\left(\frac{a}{r}\right)^{n+2}+ \\ +\left[q_n^m\cos m\phi+s_n^m\sin m\phi\right]\left(\frac{r}{a}\right)^{n-1}\}\frac{dP_n^m(\theta)}{d\theta} \tag{3.10}$$

$$B_\phi = \frac{1}{\sin\theta}\sum_{n=1}^{\infty}\sum_{m=0}^{n} m\{[g_n^m \sin m\phi - h_n^m \cos m\phi]\left(\frac{a}{r}\right)^{n+2} + \\ + [q_n^m \sin m\phi - s_n^m \cos m\phi]\left(\frac{r}{a}\right)^{n-1}\}P_n^m(\theta) \tag{3.11}$$

## 3.2 Equivalent source dipole (ESD) model

The ESD method consists in treating a material as a dipole distribution with a given thickness, and finding the resulting magnetic field outside the region magnetized. With this, we obtain the magnetic field at a constant altitude above the region where we have the dipole sources [12].

The magnetic potential, observed at $(r, \theta, \phi)$, is defined as

$$V = -\mathbf{M} \cdot \nabla \frac{1}{l} \tag{3.12}$$

Where $\mathbf{M}$ is the magnetic moment of a point dipole located at $(r_d, \theta_d, \phi_d)$. This relation is valid when there are no sources between the observation point and the dipole. The distance $l$ is defined as

$$l = \left(r_d^2 + r^2 - 2r_d r\cos(\zeta)\right)^{\frac{1}{2}} \tag{3.13}$$

Where $\zeta$ is the angle between the two position vectors, and $cos(\zeta)$ can be written

$$\cos(\zeta) = \cos(\theta)\cos(\theta_d) + \sin(\theta)\sin(\theta_d)\cos(\phi - \phi_d) \tag{3.14}$$

Re-writing the equation 3.12, we have

$$V(r, \theta, \phi) = \frac{M_r(rA_1 - r_d) - M_\theta r B_1 + M_\phi r C_1}{l^3} \tag{3.15}$$

Where the coefficients are:

$$A_1 = \cos(\theta)\cos(\theta_d) + \sin(\theta)\sin(\theta_d)\cos(\phi - \phi_d) = \cos(\zeta) \tag{3.16}$$

$$B_1 = \cos(\theta)\sin(\theta_d) - \sin(\theta)\cos(\theta_d)\cos(\phi - \phi_d) \tag{3.17}$$

$$C_1 = \sin(\theta) sin(\phi - \phi_d) \tag{3.18}$$

The total magnetic field $\mathbf{B}$ comes from the equation 3.3 in spherical coordinates,

$$\mathbf{B} = -\left(\frac{\partial}{\partial r}, \frac{\partial}{r\partial\theta}, \frac{\partial}{r\sin(\theta)\partial\phi}\right) V \tag{3.19}$$

Deriving $A_1$, $B_1$ and $C_1$ in relation to $\theta$ and $\phi$ we define,

$$A_2 = \frac{\partial A_1}{\partial\theta} = -\sin(\theta)\cos(\theta_d) + \cos(\theta)\sin(\theta_d)\cos(\phi - \phi_d) \tag{3.20}$$

$$B_2 = \frac{\partial B_1}{\partial\theta} = -\sin(\theta)\sin(\theta_d) - \cos(\theta)\cos(\theta_d)\cos(\phi - \phi_d) \tag{3.21}$$

$$C_2 = \frac{\partial C_1}{\partial\theta} = \cos(\theta)\sin(\phi - \phi_d) \tag{3.22}$$

$$A_3 = \frac{\partial A_1}{\sin(\theta)\partial\phi} = -\sin(\theta_d)\sin(\phi - \phi_d) \tag{3.23}$$

$$B_3 = \frac{\partial B_1}{\sin(\theta)\partial\phi} = \cos(\theta_d)\sin(\phi - \phi_d) \tag{3.24}$$

$$C_3 = \frac{\partial C_1}{\sin(\theta)\partial\phi} = \cos(\phi - \phi_d) \tag{3.25}$$

Finally, we can write the expressions to the three components of the magnetic field, using equations 3.15, and the partial derivatives above:

$$B_r = M_r\frac{\frac{3D_1\ F_1}{l^2} - A_1}{l^3} + M_\theta\frac{\frac{3D_1\ F_2}{l^2} + B_1}{l^3} + M_\phi\frac{\frac{3D_1\ F_3}{l^2} - C_1}{l^3} \tag{3.26}$$

$$B_\theta = M_r\frac{\frac{3D_2\ F_1}{l^2} - A_2}{l^3} + M_\theta\frac{\frac{3D_2\ F_2}{l^2} + B_2}{l^3} + M_\phi\frac{\frac{3D_2\ F_3}{l^2} - C_2}{l^3} \tag{3.27}$$

$$B_\phi = M_r\frac{\frac{3D_3\ F_1}{l^2} - A_3}{l^3} + M_\theta\frac{\frac{3D_3\ F_2}{l^2} + B_3}{l^3} + M_\phi\frac{\frac{3D_3\ F_3}{l^2} - C_3}{l^3} \tag{3.28}$$

Where, $D_1 = r - r_d A_1$, $D_2 = -r_d A_2$, $D_3 = -r_d A_3$, $F_1 = rA_1 - r_d$, $F_2 = -rB_1$ and $F_3 = rC_1$ .

## 3.3 The inverse problem

The inverse problem is an algebraic formulation of the problem that consists in obtaining the parameters of some model (SH or ESD) from measured values of $B_r$, $B_\theta$, and $B_\phi$. It is written as

$$\tilde{b} = \tilde{D}x + \tilde{\nu} \tag{3.29}$$

where $\tilde{b}$ is the vector that contains the observations, $x$ is the vector of parameters (unknowns), $\tilde{\nu}$ is the noise vector (of mean zero and covariance matrix $W^{-1}$), and $\tilde{D}$ is the function matrix that relates the vectors $\tilde{b}$ and $x$.

The matrix $\tilde{D}$, in the case of spherical harmonics is composed by the factors that are multiplying the gauss coefficients, in equations 3.9, 3.10,3.11. In the case of the equivalent dipole sources, the matrix $\tilde{D}$ is composed by the partial factors multiplying $M_r$, $M_\theta$ and $M_\phi$ in equations 3.26, 3.27, and 3.28.

To normalize the vector $\tilde{\nu}$, we multiply the equation 3.29 by $W^{\frac{1}{2}}$, giving

$$b = Dx + \nu \tag{3.30}$$

The inverse problem is solved when we find the minimum of $L(x) = \nu^T \nu$, that corresponds to the equation,

$$D^T b = D^T D x \tag{3.31}$$

### 3.3.1 Conjugate gradient approach

In fact, the computation of $D^T D$ from equation 3.31 can be very heavy, and it is better to use the conjugate gradient approach. The minimum of L is reached when it's gradient is zero, $\nabla L = 0$, that means $Dx - b = 0$.

The process is iterative, in each step k, a search direction $p_k$ is generated, and a scalar, $\alpha_k$, is sought that minimizes $L(x_k + \alpha_k p_k)$. The new solution is $x_{k+1} = x_k + \alpha_k p_k$.

The expression of $\alpha_k$ is

$$\alpha_k = \frac{r_k^T r_k}{p_k^T D^T D p_k} \tag{3.32}$$

Where $r_k$ is

$$r_k = D^T b - D^T D x_k \tag{3.33}$$

Using the matrix identity $p_k^T D^T D p_k = (D p_k)^T D p_k$ in equation 3.32, we use directly the D matrix instead of the product $D^T D$ (called the design matrix approach).

# Chapter 4

# Choice of the technique to use for Mercury

In this chapter I discuss the choice of the method I should use to model the magnetic field of Mercury. The situation we have to deal with is the following: 1) Mercury has a magnetic field, believed to be of internal origin and that probably changes with time (meaning that probably exists a secular variation), and 2) the spacecraft accumulates measures with a good signal/noise rate over a particular region of the planet, the North hemisphere.

To find a good method to compute Mercury magnetic field model in these conditions, I create synthetic magnetic field data from the only planetary magnetic field that we know well, the Earth's magnetic field. After that, I show results obtained by Benoit Langlais providing evidence that the SH model method is not appropriate for local measures of magnetic field. Finally, I present the new method developed in this thesis for a better modeling of the hermean magnetic field.

## 4.1 Magnetic field of Mercury versus Earth

Measures for the magnetic field of Mercury are not available yet, and that's why I have to create synthetic magnetic field data, to proceed with this thesis work. It is believed that the magnetic field of Mercury has an internal origin and is mainly dipolar, like the Earth's. In this section I will first describe the internal magnetic field of the Earth, and from this I will generate a synthetic magnetic field for Mercury.

### 4.1.1 Geomagnetic field models

It is the SH modeling technique explained in section 3.1 that is usually applied to the Earth. What is done is an inversion of the observations, acquired during a certain time period, from ground based stations and/or from satellites. From this inversion we obtain the Gauss coefficients for the magnetic field and for the secular variation. Differences in the data used and in the inversion techniques to get this coefficients give rise to different models for the Earth magnetic field, like gufm1, POMME4-1, IGRF-11, etc. These coefficients are used in equations 3.9, 3.10, and 3.11, in the magnetic field case. For the secular variation, we do the derivative of these equations, where the coefficients are $\dot{g}_n^m$, $\dot{h}_n^m$, $\dot{q}_n^m$, $\dot{h}_n^m$. With this equations we know the magnetic field continuously inside Earth down to the CMB, and on and above the Earth's surface up to regions of electrical current sources. With this information, we plot maps usually at the Earth's surface and at the CMB, to see the magnetic field created by internal sources (meaning that we use the first terms in equations 3.9, 3.10, and 3.11, involving $g_n^m$ and $h_n^m$). Figure 4.1 shows the maps of the radial magnetic field at those two mentioned surfaces, for model gufm1.

#### Field spectrum

The way to represent indirectly the magnetic field of the Earth, is to plot the mean-square value over the surface $S(r)$ of the magnetic-field intensity produced by degree n, the harmonics $R_n(r)$. This quantity verifies,

$$\langle |\mathbf{B}|^2 \rangle_{S(r)} = \sum_{n=1}^{\infty} R_n(r) \tag{4.1}$$

where the set of $R_n(r)$ values for n=1,2,3... at a fixed radius is called the Mauersberger-Lowes (ML) spectrum on $S(r)$, and its expression is,

$$R_n(r) = \left(\frac{a}{r}\right)^{2n+4} (n+1) \sum_{m=0}^{n} \left[ (g_n^m)^2 + (h_n^m)^2 \right] \tag{4.2}$$

The equivalent expression for the SV spectrum is given by,

$$F_n(r) = \left(\frac{a}{r}\right)^{2n+4} (n+1) \sum_{m=0}^{n} \left[ (\dot{g}_n^m)^2 + \left(\dot{h}_n^m\right)^2 \right] \tag{4.3}$$

Figure 4.2 shows two ML spectra, at the Earth's surface and at the core mantle boundary (CMB), using the POMME4-1 model. In figure 4.2 a), where $r = a$ (the

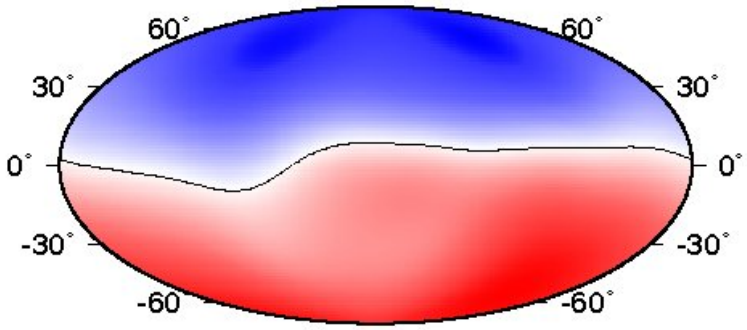


(a)

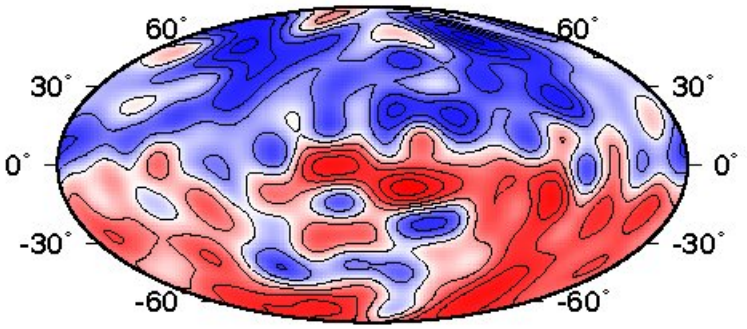


(b)

Figure 4.1: Maps of the radial magnetic field obtained from model gufm1: a) at the Earth's surface; b) at the CMB.

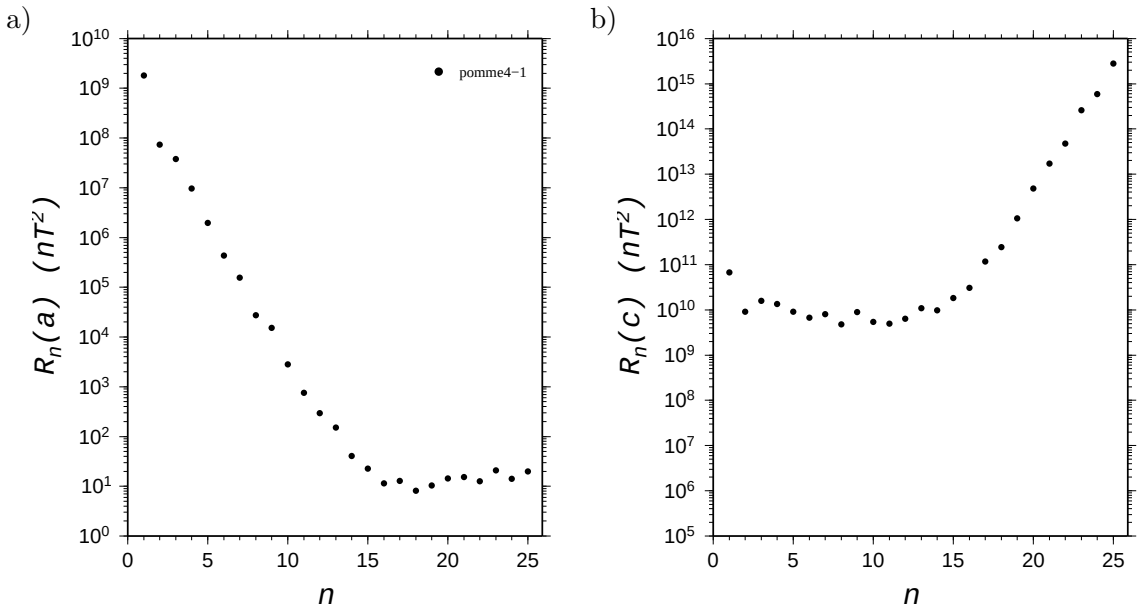


Figure 4.2: Geomagnetic field spectrum or Mauersberguer-Lowes spectrum, up to degree 25, computed from POMME4-1 model: a) at the Earth's surface; b) at the CMB.

Earth's radius), the dipole term ($n = 1$) stands alone, and there is an apparent break in spectrum near degree 14. The break is interpreted as the transition between core field domination ($n \leq 13$) to crustal field domination ($n \geq 15$). In reality, the crustal field contributes to all degrees, but is imperceptible to the first ones due to the much stronger core's magnetic field. This means that the presence of crustal magnetic fields create a limitation on the accuracy of estimates of the core field. In figure 4.2 b) we have $r = c$, where $c$ is the core-mantle boundary (CMB) radius. As we can see, the dipole term still dominates and a break occurs at the same degree referred above. But the Mauerberger-Lowes spectrum of the magnetic-field at the CMB is now approximately horizontal for degrees $n \leq 13$ representing the internal source, and shows a positive trend for degrees $n \geq 15$.

Figure 4.3 shows the secular variation spectrum at the Earth's surface. From this figure we see that the magnitude of the secular variation is much lower than the magnitude of the magnetic field. Curiously, it is the second degree that has the highest magnitude value, and not the first degree like for magnetic field.

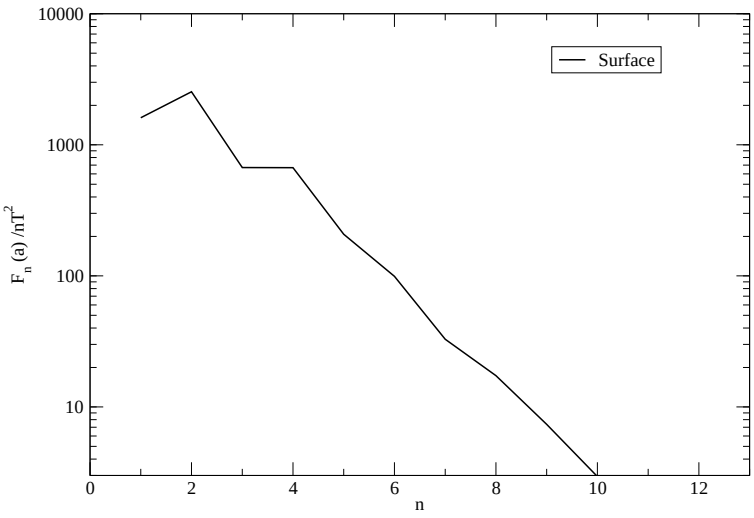


Figure 4.3: Spectrum of the secular variation at the Earth's surface $r = a$. The coefficients used are from the model POMME4-1.

### 4.1.2 The models for Mercury

Comparing the internal structure of Earth and Mercury, as I show in figure 4.4, we see that, putting both planets at same scale, the core's size of Mercury is bigger. That is, the core's size of Earth is 55% of the planet radius, while the core's size of Mercury is 74% of the planet radius. So, to create the hermean's magnetic field from the Earth's field, we have to find where would be the hypothetical Mercury's surface if the planet had the Earth's core size. This is done simply by writing $\frac{c}{R_M} = 0.74$.

Using equation 4.2 with $r = R_M$, where $R_M$ is the hypothetical Mercury's surface at Earth, and making equal to the same equation where the term $(\frac{a}{r})^{2n+4}$ is made 1 (because the surface reference radius is now equal to $R_M$), we get the gauss coefficients for this hypothetical Mercury which would have its surface inside the Earth's mantle. The same is done for the secular variation. Figure 4.5 and figure 4.6 show the ML spectra for the MF and SV when $r = R_M$, respectively. The value of $R_M$ is not fixed, as we don't know Mercury's core radius with certainty. We can estimate a range between [1800 $km$, 2200 $km$] for Mercury core's radius, from measurements of the mass and rotation of the planet [3]. In this thesis work, I will use $R_M = 4740$ $km$ (corresponding to a core's Mercury radius of 1800 $km$), and leave for future work the search of the radius's value that best explains the data, when these will be available.

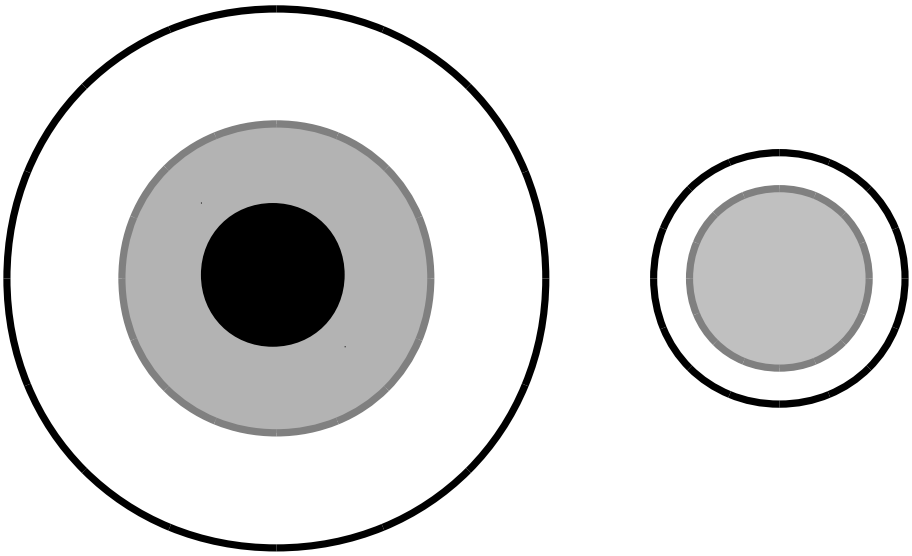

Figure 4.4: Internal structures of the two planets Earth (left) and Mercury (smaller planet, right). The main difference is the relative size of the core, which almost takes account of the total planet in the case of Mercury. Notice that Mercury doesn't have a solid core like the Earth (black circle).

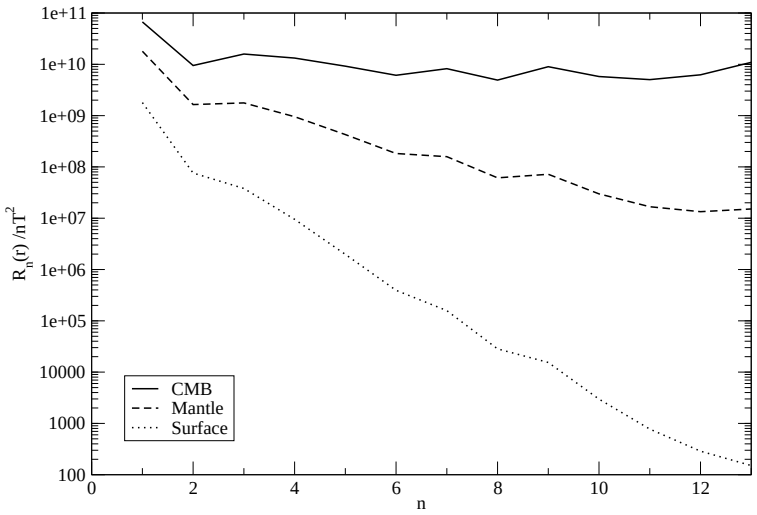


Figure 4.5: Magnetic field spectrum computed with POMME4-1, for the Earth's surface (dotted line), for the CMB (solid line), and for $R_M$ (dashed line).

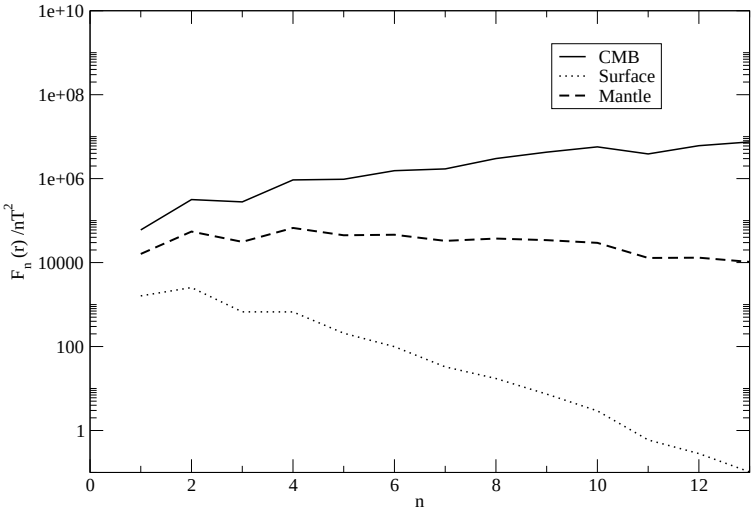


Figure 4.6: Secular variation spectrum computed with POMME4-1, for the Earth's surface, for the CMB, and for $R_M$.

One more step is needed, to put the coefficients to Mercury's dipole coefficients scale. That is possible, because we know the first SH coefficient of Mercury for the main field, from Mariner 10 flybys, and from the first MESSENGER's flybys [13]. For the secular variation of Mercury, we ignore it's characteristic timescale and amplitude, and it is believed that at Mercury the secular variation is much smaller than at Earth. Note that even if there exists a secular variation we can't possibly see it, if it is very slow. That is, we won't be able to measure Mercury's secular variation if the characteristic timescale is longer than the mission period or if the instruments precision is inferior to the intensity of magnetic field variations during the mission period.

Table 4.1 shows the values obtained in [13] for two models 5 and 6 separately, and its average. Models 5 and 6 are SH quadrupolar ($n = 2$) internal models. Model 5 results from the SH analysis (SHA) treatment for the external field, and model 6 obtains the external field from magnetopause currents, for a given shape and an approximate estimate of the planetary magnetic field. To put the Gauss coefficients inside mantle's Earth at Mercury's scale, I use a factor, $f$, defined as,

$$f = \frac{g^0_{1M}}{g^0_{1\oplus}} \tag{4.4}$$

Table 4.1: Average of Mercury's coefficients for models 5 and 6 from [13]. All coefficients are in units of nT for spherical harmonic expansion with distance normalized to the mean Mercury radius.

| models | $g_1^0$ | $g_1^1$ | $h_1^1$ | $g_2^0$ | $g_2^1$ | $g_2^2$ | $h_2^1$ | $h_2^2$ |
|---|---|---|---|---|---|---|---|---|
| 5 Quad. | -213 | -4 | 7 | -66 | 9 | 4 | 5 | -4 |
| 6 Quad. | -182 | -15 | 9 | -108 | 10 | 2 | 6 | -15 |
| Average | -198 | -10 | 8 | -87 | 10 | 3 | 6 | 10 |

where $g^0_{1\,M}$ is the first SH coefficient for Mercury, and $g^0_{1\oplus}$ is the first coefficient for Earth.

The model for the main field for Mercury keeps the first coefficient $g_1^0$ measured in Mercury with a lower error, and the following coefficients up to degree $n = 10$ are those in the mantle's Earth multiplied by the factor, $f$, equation 4.4. For the secular variation, we use all the values computed in mantle's Earth, divided by a factor 10. The model is presented in Appendix A.

Figure 4.7(a) shows the synthetic magnetic field of Mercury, and figure 4.7(b) shows the secular variation during one year.

## 4.2 Tests of the SH method

In this section I will present results from Benoit Langlais showing that the SH model method is not appropriate for inverting measures of the magnetic field on a limited region, where we expect MESSENGER instruments to get a good rate signal/noise (North hemisphere). The selection method is explained later in section 6.1.1.

Benoit Langlais used an iterative method from an algorithm described in [14]. Here he uses as the departure model, one geomagnetic field model modified to Mercury's scale. He tested different truncations, of degrees $(1, 2, 3, 4, 5, 10)$ for the main field, and in each case considered two situations: with or without a secular variation with the same degree. Figure 4.8 shows the root mean square (rms) of the differences between the obtained and measured magnetic field values at the orbit locations (also named misfit). Results are shown for each degree of truncation.

From figure 4.8 we see that as the degree $n$ increases, the rms decreases. No degrees higher than 5 are shown because for degree 5 without secular variation it is needed

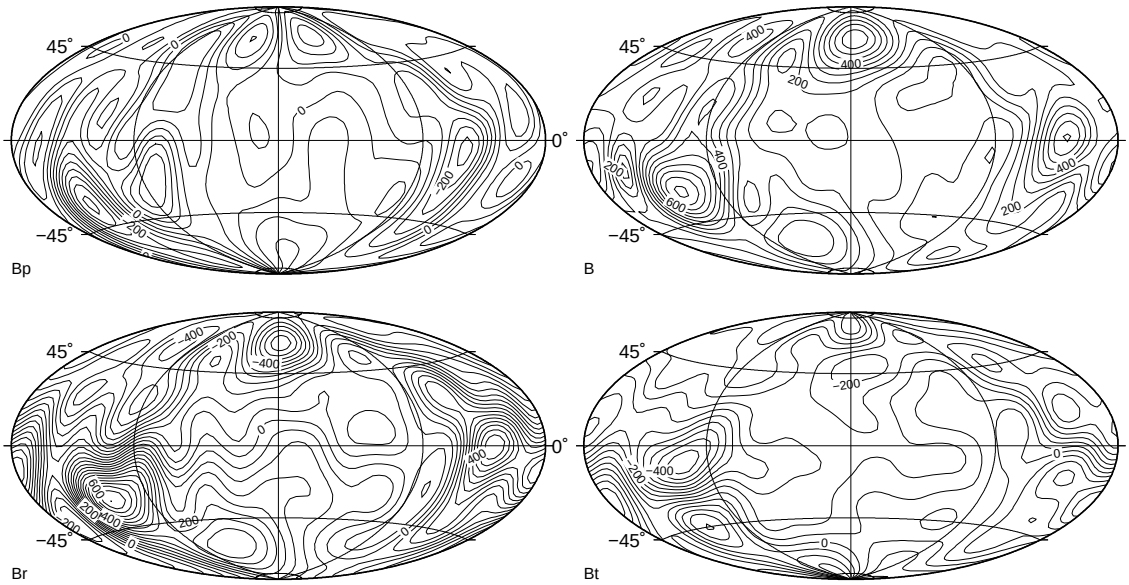


(a)

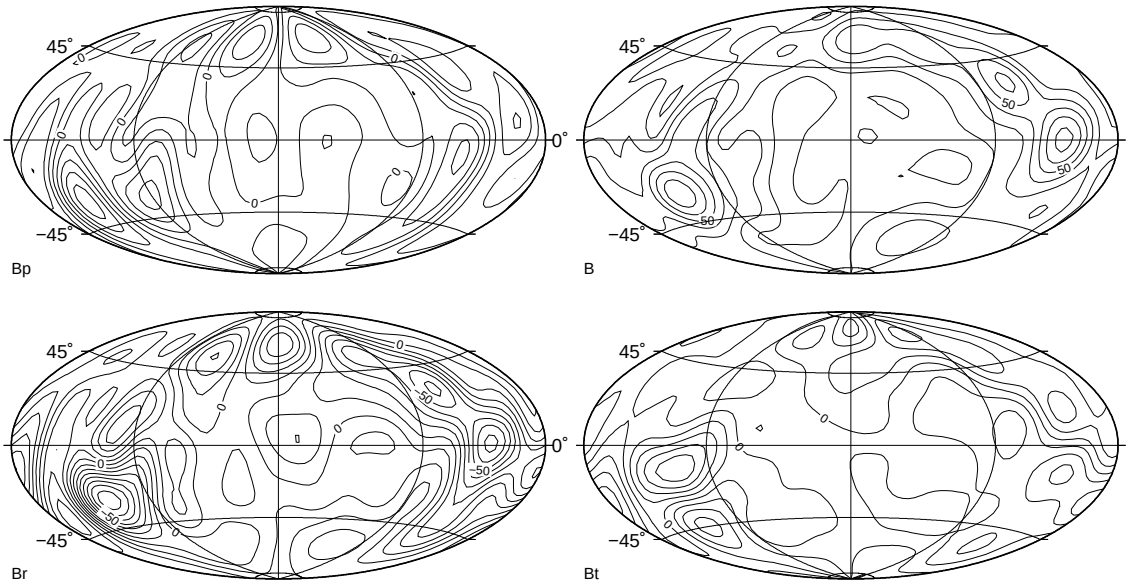


(b)

Figure 4.7: Maps for: a) synthetic magnetic field for Mercury at an altitude of 300 $km$ from Mercury's surface in nT, interval between contours is 50 nT, and b) synthetic secular variation in nT/yr at the same altitude, interval between contours is 10 nT/yr.

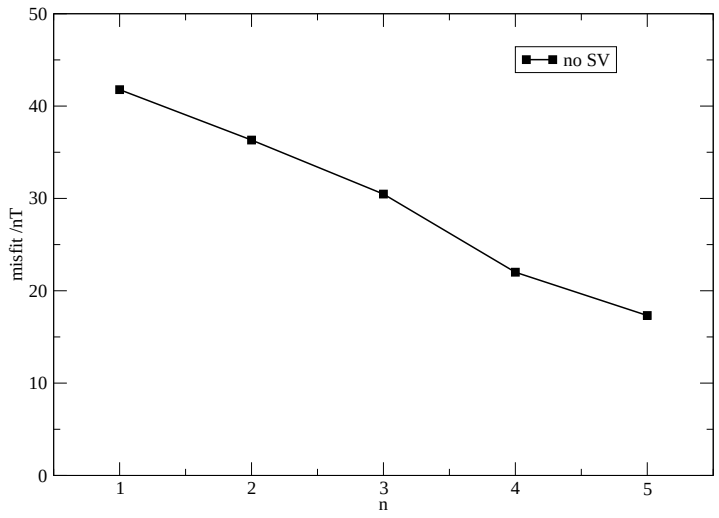


Figure 4.8: Misfit as a function of the degree n, for the case when the model has no secular variation.

3000 iterations, which is already an heavy computer calculation. The convergence is more and more difficult with increasing n, and there is no convergence at all for degree 10.

Figures 4.9 and 4.10 show the ML spectrum for the magnetic field and for the secular variation, respectively. Here, are represented the different SH models that have converged. Comparing with the initial model for Mercury (black lines), we can see that there are no models that can represent the initial one.

We use equation 4.5 from [15] to compare both models ( Mercury's initial model and the different models resulting from inversion).

$$\left\langle F^2 \right\rangle = \sum_{n=0}^{n*} (n+1) \sum_{m=0}^{n} \left[ (\triangle g_n^m)^2 + (\triangle h_n^m)^2 \right] \tag{4.5}$$

where $\triangle g_n^m$ and $\triangle h_n^m$ are the differences in the Schmidt-normalized spherical harmonic coefficients from the two models being compared, and n* is the maximum degree and order of the analysis.

We obtain huge differences for the main field and for the secular variation. The model with truncation degree $n = 2$ for MF and SV, is the one that shows a lower $\left\langle F^2 \right\rangle$ value, but still high ($\sim 90\ nT$). This model is showed in table 4.2.

If we compare with the initial model for Mercury, for the same degrees, we obtain

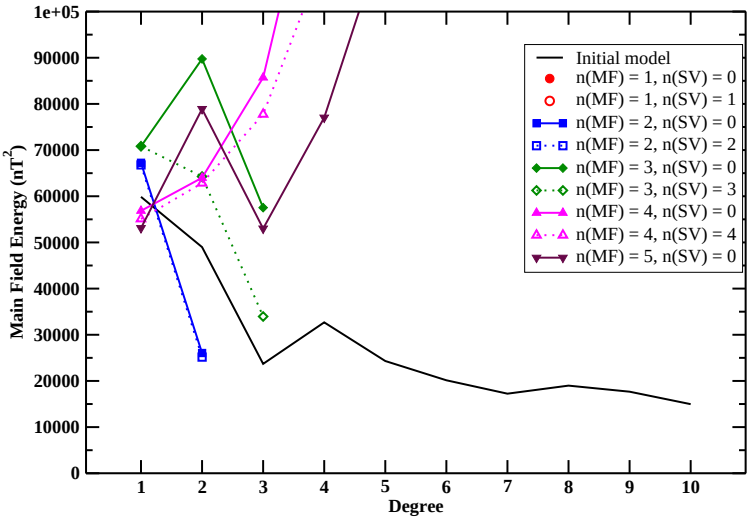


Figure 4.9: ML spectrum for different SH computed models, differing in the degree of truncation. The initial model for Mercury from where the synthetic data was computed, is also represented for comparison.

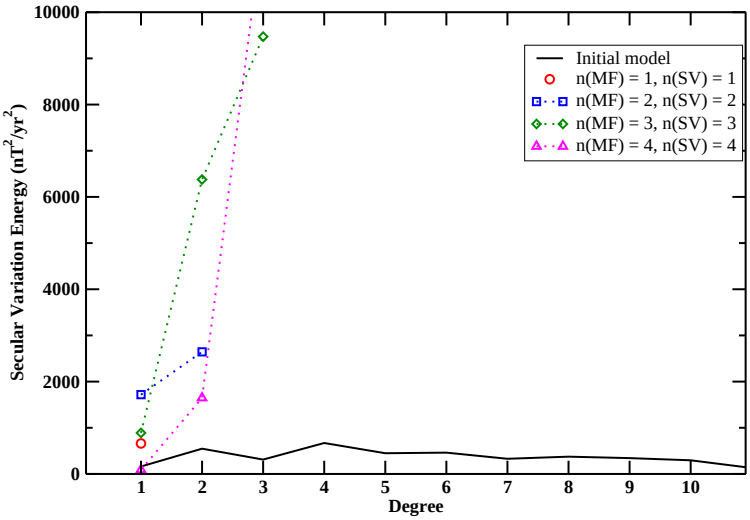


Figure 4.10: Secular variation spectrum for the different inverted models, of different truncation degrees. The model for Mercury is also represented, for comparison.

Table 4.2: SH model with truncation $n = 2$ obtained after the inversion.

| n | m | g | h | $\dot{g}$ | $\dot{h}$ |
|---|---|---|---|---|---|
| 1 | 0 | -178.68 | | 4.57 | |
| 1 | 1 | 24.61 | -29.30 | -4.43 | -28.61 |
| 2 | 0 | 50.12 | | -6.36 | |
| 2 | 1 | -0.64 | -59.20 | 0.61 | 16.38 |
| 2 | 2 | -7.67 | -48.09 | -21.28 | -10.92 |

Table 4.3: Differences in percentage between the SH model ($n = 2$) obtained after inversion, and the initial model for Mercury.

| n | m | g | h | $\dot{g}$ | $\dot{h}$ |
|---|---|---|---|---|---|
| 1 | 0 | -4.2% | | 20.5% | |
| 1 | 1 | 40.5% | 96.0% | 201.8% | 307.5% |
| 2 | 0 | 24.9% | | 1.5% | |
| 2 | 1 | 104.3% | 40.0% | 128.2% | 256.3% |
| 2 | 2 | 164.3% | 13.9% | 277% | 104.9% |

the differences in percentage shown in table 4.3.

As a conclusion, using the standard SH methods for obtaining inverted models, we just obtain an acceptable error (5%) for the centered axial dipole ($g_1^0$), the other coefficients being very badly recovered. For the secular variation the results are still worse.

## 4.3 The new method: time variable ESD

In the previous section we tested the most standard inversion method used when computing time-varying magnetic field models for the Earth (time dependent SH), assuming we had the data distribution conditions for Mercury. We confirmed that the method doesn't work if we don't have a globally distributed measures set. The Equivalent Source Dipole (ESD) method has been previously used for modelling the crustal fields of Mars [12]. It has been used in situations when the field is modeled in

a circumscribed region, but never before for modeling the secular variation. In this thesis, we implement a time variable Equivalent Source Dipoles.

This new method doesn't describe only the three magnetic field components by the three magnetization components $M_r$, $M_\theta$ and $M_\phi$, but also the temporal variation of the magnetic field (or secular variation) by the temporal variation of the three magnetization components, $\dot{M}_r$, $\dot{M}_\theta$, and $\dot{M}_\phi$. This improvement of the method ESD, requires to fit six parameters for each dipole, instead of three as I show in section 3.2. In this case the magnetization is a linear function of the time as,

$$M(t) = M_0 + M_1 \times t \tag{4.6}$$

where $M_0$ is the magnetization at a reference time, and $M_1$ is the rate of time evolution of the magnetization.

In the next chapters I will use this new method and show how it is applied to the specific problem in my hands.

# Chapter 5

# Validation of the new method

The computer program used in this thesis was developed initially by Purucker et al. ([16]), and was created to produce a constant altitude map of the magnetic field of Mars, using an equivalent source dipole approach, from Mars Global Surveyor (MGS) spacecraft magnetic observations. In the first version, the program used only the radial component of the magnetic field measured at low altitudes, to compute the radial magnetization only. Later, the program was extended ([12]) by introducing the three components of the magnetic field observations to constrain the three magnetization components of the equivalent dipole sources.

In this thesis, the program was again improved, by Benoit Langlais, to take into account the variation in time of the three magnetic field components and of the equivalent dipole sources.

## 5.1 The method

The method consists in two parts: 1) the inversion of the magnetic field data (synthetic, in this study, measured when MESSENGER data will be available) to a distribution of magnetization, and 2) the direct calculation to predict the magnetic field due to to the resulting distribution of dipoles with known magnetizations in any location above that distribution.

Figure 5.1 shows a scheme of the program used. In the first part I use the program to invert the three components of the magnetic field measures ($B_r$,$B_\theta$, $B_\phi$) and the three components of the secular variation ($\dot{B}_r$,$\dot{B}_\theta$, $\dot{B}_\phi$) using the information of the dipole distribution on a sphere (more details in section 5.1.1) previously calculated. This allows to obtain the model, that is the magnetization $M(r, \theta, \phi, t)$, (where the

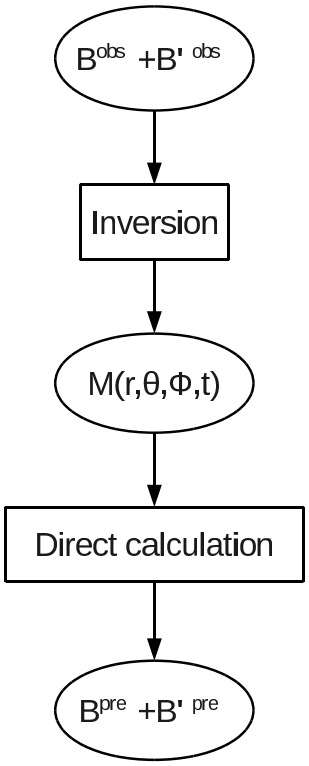


Figure 5.1: Scheme of the program.

time dependence is assumed linear) distributed in the dipole locations given. This is an iterative process (see chapter 3.3), and the inversion is stopped after 100 iterations (except when I am testing the program, in that case I can use more iterations). Then, in the second part I use the program to predict the magnetic field observations using each iteration of each magnetization solution.

As we know that the solution is non-unique, a criteria is usually defined to decide which solution should be trusted, based on the evolution of the standard error (also named 'misfit') and the correlation between observations and predictions. The standard error is defined as the root mean square of the sum of the squared differences between observed and predicted magnetic measures,

$$\sigma_B = \sqrt{\frac{\sum_{i=1}^{n}(B^{obs} - B^{pre})^2}{N}} \tag{5.1}$$

Where $B^{obs}$ and $B^{pre}$ are the observed and predicted values, respectively, and $N$ is the total number of measurements (predicted or observed).

The correlation of the magnetic field is defined as,

$$\chi_B = \frac{n\sum(B^{pre}B^{obs}) - \sum(B^{pre})\sum(B^{obs})}{\sqrt{[n\sum(B^{pre})^2 - (\sum B^{pre})^2][n\sum(B^{obs})^2 - (\sum B^{obs})^2]}} \tag{5.2}$$

### 5.1.1 Input parameters and data

The input data is the magnetic field, measured or synthetic (calculated from the Earth's model at Mercury's scale, as explained in section 4.1). The input parameter is the dipole distribution.

#### Dipole distribution

The dipole distribution is chosen taking into account the different methods of spherical tesselations. The dipole geographical distribution should be as homogeneous as possible, in order to minimize the sources of instabilities [17]. There are many studies about the most homogeneous distribution on the sphere, and in this work the method named polar coordinate subdivision is chosen [18]. In [19], the author prove that this is one of the studied distributions that shows lower magnetic field values over the sphere, when it is applied to the Runcorn's theorem conditions, with a spherical shell and an internal dipole field, for which case the theoretical result is a null field outside the shell.

The generating technique consists in considering $(N-1)$ equally spaced latitude bands $L_j$ corresponding to $\varphi = \phi_j = \frac{\pi j}{N} - \frac{\pi}{2}$ where $j = 1, ..., (N-1)$. On the latitude $L_j$, we place $N_j$ equally spaced points, starting at $\theta = 0$, where $N_j$ is given by

$$N_j = \lfloor \frac{1}{2} + \sqrt{3} n_d \cos\phi_j \rfloor \tag{5.3}$$

On alternate latitudes, a phase shift is imposed to make the configuration more symmetric [18].

It is now defined a dipole parameter, $n_d$. This number can vary as we wish, and is related to the total number of dipoles on the sphere, $m$. Increasing the dipole parameter is the same as increasing the total number of dipoles, and leads to a decrease of the mean distance between them. Table 5.1 shows us the dependence between the dipole parameter and the total number of dipoles and the mean distance.

Figure 5.2 shows us an example of a dipole distribution with a dipole parameter $n_d = 15$. As we can see, the distribution is homogeneous.

Table 5.1: Values for the dipole grid at a depth of 640 $km$ from Mercury's surface (radius of 1800 $km$). $m$, $d$, and $n_d$ are the total number of dipoles, mean spacing, and the dipole parameter, respectively.

| $n_d$ | $m$ | $d/^\circ$ |
|---|---|---|
| 13 | 167 | 15.72 |
| 14 | 194 | 14.58 |
| 15 | 223 | 13.60 |
| 16 | 256 | 12.69 |
| 17 | 292 | 11.89 |
| 18 | 328 | 11.21 |
| 19 | 368 | 10.59 |
| 20 | 408 | 10.06 |
| 21 | 451 | 9.56 |
| 22 | 496 | 9.12 |
| 23 | 543 | 8.72 |
| 24 | 596 | 8.32 |
| 25 | 648 | 7.98 |
| 26 | 702 | 7.67 |
| 27 | 756 | 7.39 |
| 28 | 816 | 7.11 |
| 29 | 881 | 6.84 |

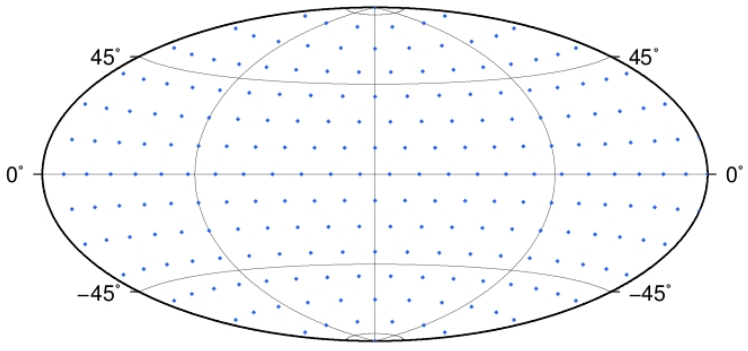


Figure 5.2: Distribution of dipoles on a spherical surface, with dipole parameter of $n_d = 15$, that means 223 total number of dipoles. Hammer projection is used.

## 5.2 Testing the Program

In this section I validate the use of the computer program for this thesis work, and confirm that it gives the desired results. Here, my main concerns are: i) to verify how the program works after including the secular variation; ii) to estimate what resolution of the model I should use; and iii) to check the effect of the noise in the data.

I call the attention for the terminology used in this thesis: $B(MF)$ refers to the internal or main field, $\mathbf{B}$, $B(SV)$ refers to the secular variation of the main magnetic field, $\dot{\mathbf{B}}$, and $\mathbf{M}$ refers to the magnetization model.

Notice that for testing the program, I use synthetic data predicted on a regular grid or at spacecraft locations.

### 5.2.1 Validation

To confirm that the method works, I performed different tests. The tests consist basically in observing the behavior of the misfits (see equation 5.1) when following the main sequence of computations or when following two secondary sequences. I will designate a sequence of computations by 'path'. The main path is the one where we invert the space and time varying magnetic field, $B(r, \theta, \phi, t)$ or $B(MF + SV)$. The secondary paths consist in the inversion for the magnetic field, $B(MF)$, or for the secular variation $B(SV)$, separately. Moreover, in the main path I separate the model $M(MF + SV)$ into its two components ($M^*(MF)$ and $M^*(SV)$), to generate fields that are compared with the secondary's input data, B(MF) and B(SV), respectively. The set of all different paths are shown in figure 5.3.

To calculate all the misfits, I follow all the possible paths, starting from a given initial data set. The magnetic field data is a grid with resolution of 4 degrees in latitude and longitude, with altitudes of $300km$ and $500km$ from the surface. The dipoles are distributed at a depth of $640km$ from the surface, and have a dipole parameter of $n_d = 15$.

Figure 5.4 shows the misfits for the radial component, $B_r$ (following the scheme of figure 5.3) and also the correlation coefficient for $B_r(MF + SV)$. From figure 5.4(a) it is concluded that after about 60 iterations, the misfit converges to a value near zero (in the preceding iterations, the program tries to fit the magnetic field to the different dipole locations), and that the correlation coefficient stabilizes near unity after about 15 iterations. The zoom-in of figure 6.14(a) shows that the separate magnetizations

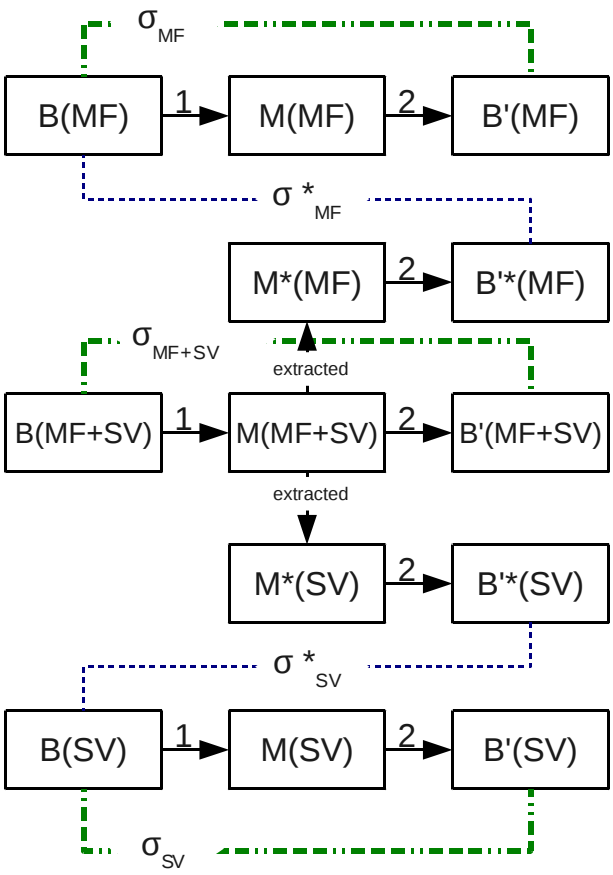


Figure 5.3: Scheme of different possible sequences of computations or paths. The main path consists in: inversion of the measured magnetic field and secular variation, $B(MF + SV)$, into a magnetization model, $M(MF + SV)$, and calculation of the magnetic field with secular variation from that model $B'(MF + SV)$. The misfit (equation 5.1) is represented by $\sigma_{MF+SV}$. In this path, there are also two ramifications, that is the separation of the magnetization $M(MF + SV)$, into the time constant component, $M^*(MF)$, and it's secular variation, $M^*(SV)$. They are then used to generate a magnetic field ($B'^*(MF)$) and a secular variation field ($B'^*(SV)$). The associated misfits, $\sigma^*_{MF}$ and $\sigma^*_{SV}$ are also calculated. Numbers 1 and 2 refer to the inversion and the direct calculation, respectively. The secondary paths work in the same way as the main path, but for the magnetic field, $B(MF)$ and for the secular variation, $B(SV)$, in separate.

$M^*(MF)$ and $M^*(SV)$ need more iterations to stabilize. Moreover, the misfits of the secular variation (both by the secondary path and by the ramification of the main path), become stable near zero, contrary to the magnetic field, that become stable at about 2 $nT$.

I should choose the best solution, due to the existence of many possible solutions in a sort of practical non-uniqueness. It is created a criteria based on the evolution of the misfit, to decide at which iteration we may accept the solution. I defined the criteria (I usually call it of 'relative evolution') as,

$$\sigma_{Bi-1} - \sigma_{Bi+1} < 0 \tag{5.4}$$

This criteria defines the iteration number when the misfit starts growing up, after being continuously decreasing. In figure 5.5 is represented the relative evolution (equation 5.4) as a function of the iteration number for all paths. After iteration 60, the values of the relative evolution become small, except for the extracted secular variation which shows more variations. That is because during the inversion of the main path, the algorithm gives a bigger importance to the fit of the main field than to the fit of the secular variation, due to the larger value of the main field (relative to the values of the secular variation). Because of this, some information on the secular variation data is lost, which can not be retrieved from the extracted magnetization $M^*(SV)$. In fact, it is verified that the extracted secular variation never fully converge before 1000 iterations.

Table 5.2 shows the iteration numbers when the criteria of equation 5.4 is verified, for the different paths. Note that as the misfit is closer to zero and the correlation coefficient closer to unity, the fit is better. At first view, it seems that the criteria is attained at very different iteration numbers making it difficult to choose one. When we look closer, we see that the criteria for the magnetic field with secular variation ($B(MF+SV)$) is found after the break iteration number for the magnetic field ($B(MF)$ alone). That, is easily understood, because the program is inverting six components (of magnetic field plus secular variation) instead of only three components (of magnetic field). For the secular variation, $B(SV)$, the criteria isn't really appropriate, because it stops too late the iterative procedure. Regarding the quantities that were extracted, the magnetic field, $B^{ext}(MF)$, stops at iteration number close to the secondary path, what is expectable. And for the secular variation extracted, $B^{ext}(SV)$, it stops too early, confirming that the program gives more importance to higher values during the inversion.

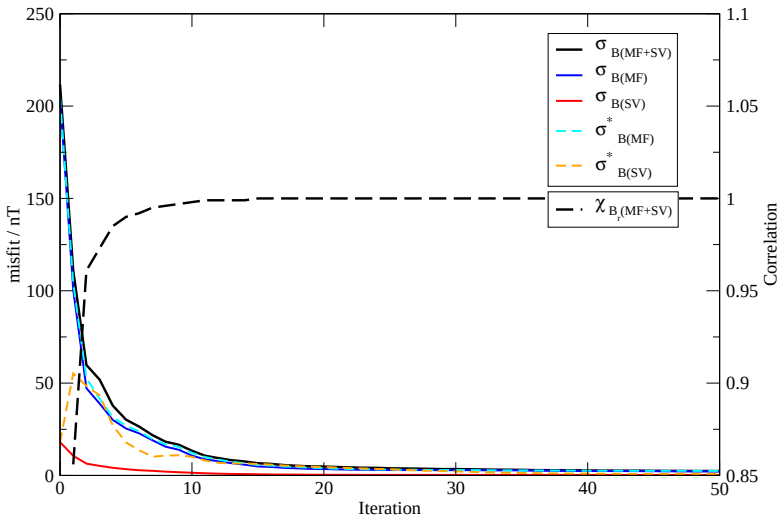


(a)

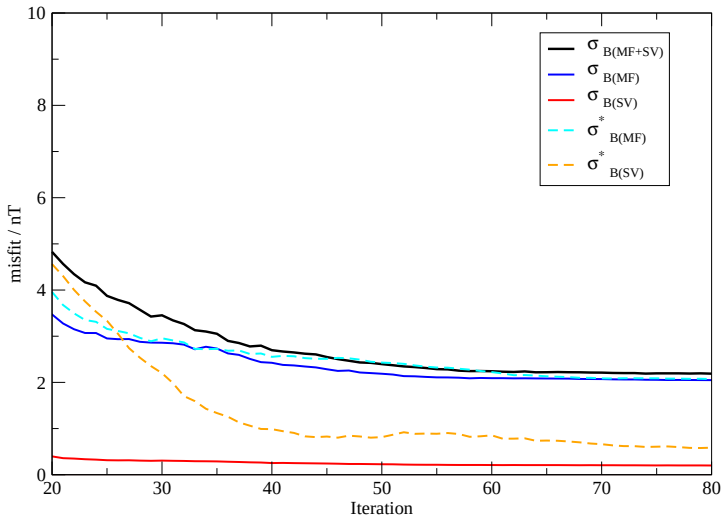


(b) Zoom of figure (a).

Figure 5.4: Plots of the misfits of the radial magnetic field, for all test paths. $\sigma_{MF+SV}$, $\sigma_{MF}$, and $\sigma_{SV}$ are the main and secondary misfits, and $\sigma^*_{MF}$ and $\sigma^*_{SV}$ are the misfits of the ramifications (see figure 5.3). In (a), it is represented also the correlation coefficient of the radial magnetic field and secular variation, $\chi_{B_r(MF+SV)}$. Dipole parameter is $n_d = 15$.

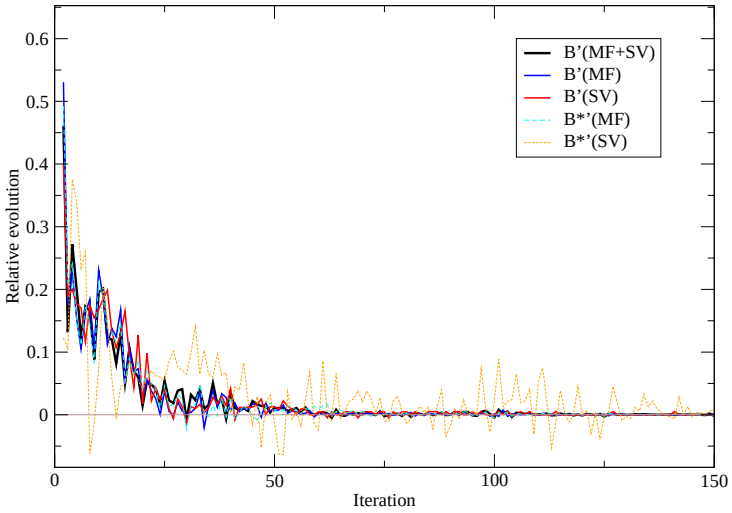


Figure 5.5: Relative evolution (equation 5.4) for all paths, of the radial magnetic field obtained. Dipole parameter $n_d = 15$.

Table 5.2: Misfit and correlation for the three components of the magnetic field, when the criteria is verified using the radial magnetic field.

| | | Misfit /nT | | | Correlation | | |
|---|---|---|---|---|---|---|---|
| Path | Iteration | $B_r$ | $B_\theta$ | $B_\phi$ | $B_r$ | $B_\theta$ | $B_\phi$ |
| $MF + SV$ | 62 | 2.226 | 1.326 | 1.004 | 1 | 1 | 1 |
| $MF$ | 33 | 2.717 | 1.591 | 1.051 | 1 | 1 | 1 |
| $SV$ | 173 | 0.182 | 0.089 | 0.102 | 1 | 1 | 1 |
| $MF^{ext}$ | 29 | 2.890 | 1.843 | 1.339 | 1 | 1 | 1 |
| $SV^{ext}$ | 8 | 10.128 | 6.567 | 6.475 | 0.905 | 0.895 | 0.899 |

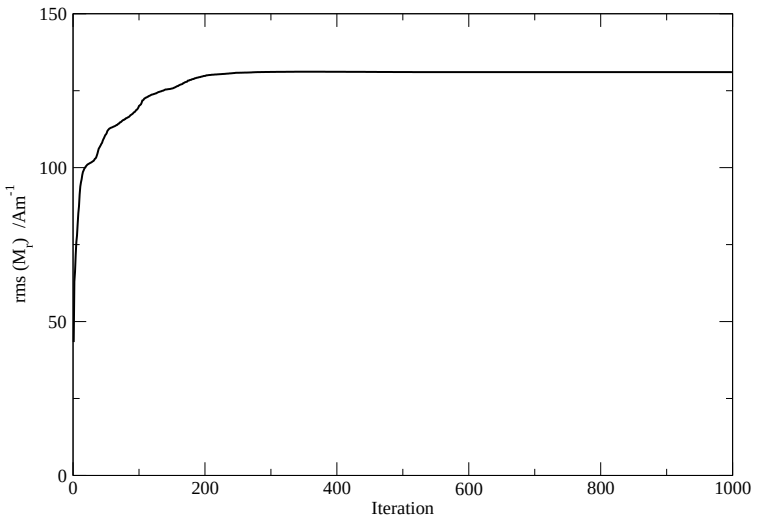


Figure 5.6: Root mean square of the radial magnetization, for the secondary path starting with $B(MF)$.

One more test is done concerning the evolution of the root mean square (rms) of the radial magnetization of the magnetic field, $M(MF)$,

$$rms(M_r) = \sqrt{\frac{(M_r)^2}{m}} \tag{5.5}$$

where m is the total number of dipoles.

Figure 5.6 shows that the rms of the magnetization stabilizes after iteration 275. Previously, I decided to stop much earlier, where the misfit stabilizes (see table 5.2). This option can be justified as while the rms of the magnetization is growing up, the program is trying to put more energy in the solution, trying to reduce the misfit. Nonetheless, the same misfit had already been obtained with lower magnetization (lower energy). Probably this is a question of non uniqueness of the problem and we choose simple (less energetic) solutions.

### 5.2.2 Resolution

The resolution of the dipole distribution affects the inversion significantly, and consequently the final results. In this section, I will verify which resolution should I take, for using in the next chapter. The resolution of the dipole distribution is directly

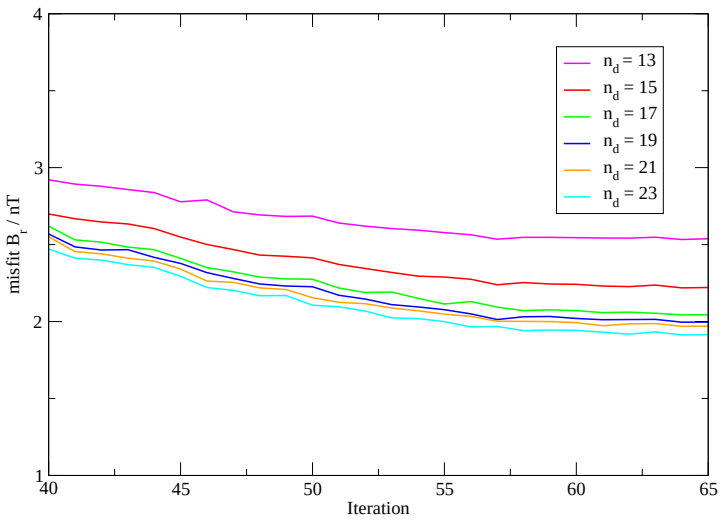


Figure 5.7: Misfit of the radial component for the main path starting with $B(MF + SV)$, when using different dipole parameters, $n_d$. The grid of dipoles is at depth of $640km$ corresponding to a core radius of $1800km$.

associated to the dipole parameter $n_d$, or the mean spacing between dipoles, $d$ (see table 5.1). Figure 5.7 shows the misfits of the magnetic field and secular variation (in the main path), depending on the different dipole parameters. Here we can observe that, when the dipole parameter increases the misfit decreases, as expected. The question is: when is the solution satisfying enough? For sure that as more dipoles are used in our distribution and the resolution is improved, the misfit is reduced, but that requires more computational memory and time, and is probably not so compensatory. More precisely, while the misfit using dipole parameters 13 and 15 is always clearly above 2 $nT$, it is not so different when choosing dipole parameter 17 or 23. For getting a balance between low misfits and reduced computer calculation time, I chose the dipole parameter $n_d = 21$, for the calculations in the next chapter.

Now, I apply the same criteria introduced in the previous section, equation 5.4. Figure 5.8 shows the relation of the break iteration when the criteria is valid, to each dipole parameter, $n_d$. We see that as we increase the dipole parameter (increase the total number of dipoles $m$), the magnitude of the misfit chosen by the criteria decreases.

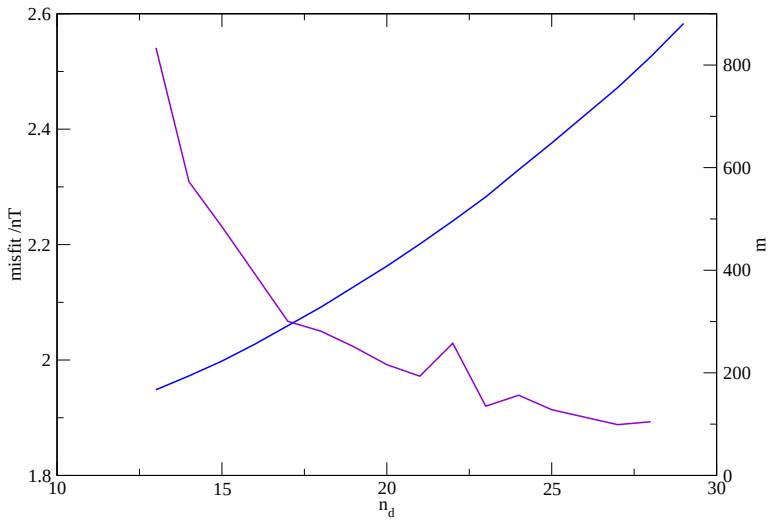


Figure 5.8: Value of the misfit with a break iteration chosen by the criteria (equation 5.4), depending on the dipole parameter, $n_d$, (purple curve). It is also represented the variation of the total number of dipoles, $m$, with the dipole parameter (blue curve).

### 5.2.3 Noise

I add noise to the data, because it is known that the spacecraft measurement have always noise, either due to limited precision and accuracy of the instruments, or to the superposition of external contributions due notably to the magnetosphere. Being closer to the Sun, Mercury is subject to a higher flux of particles of the solar wind, and the error associated with the external field is bigger.

To create the synthetic data with noise, I add a white noise, of mean zero. To see the behavior when the data have noise, I add different intensities of noise with variance: 2 $nT$, 5 $nT$ and 10 $nT$. Figure 5.9 shows a scheme of the sequence of computations done. Firstly, I add noise to the initial magnetic field synthetic measures, and after that I proceed as in section 5.2.1.

The misfits are represented in figure 5.10, for each noise level n. As we can see, the misfit at noise level n, $\sigma^n$, converges to approximately the value of the noise. Moreover, higher is the noise, faster is the convergence of the misfit. If we look to the misfit between the input data with noise and the results, $\sigma^{n'}$, it is very similar to the misfit without noise.

In conclusion, the method works as expected, except for one issue. Accordingly,

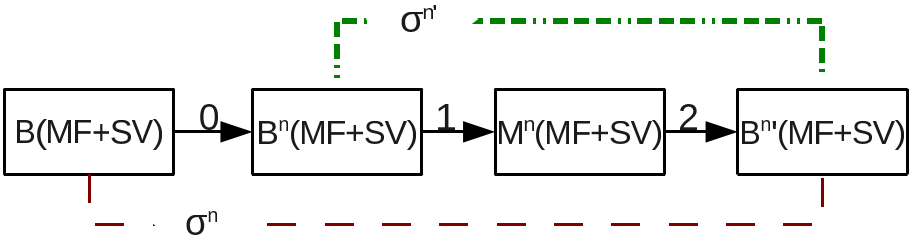


Figure 5.9: Scheme of the path used to test the effect of noise. For the same predicted data, there are two misfits to consider: when we compare the predicted magnetic field with the initial data with noise, $\sigma^{n'}$ and without noise, $\sigma^{n}$. The numbers 0, 1, and 2 mean that noise is added (0), the inversion is done (1), and the direct calculation is done (2).

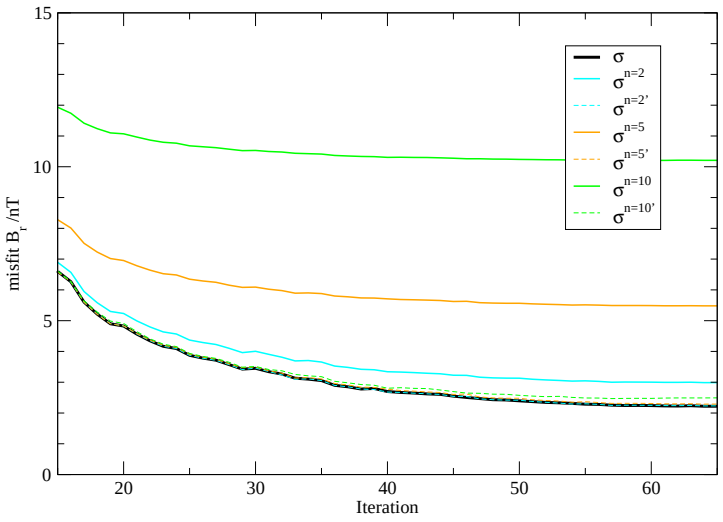


Figure 5.10: Misfit of the radial component of the main path, $B(MF + SV)$, with different noises. The misfit without noise is also represented (thick curve) to give a term of comparison. The grid of dipoles is at a depth of $640km$ corresponding to a radius core of $1800km$, with dipole parameter of 15.

as the dipole parameter $n_d$ increases the misfit is improved, and as the noise increases the misfit becomes worse. However, there still remains a problem to solve for the simultaneous inversion of the MF and SV, since we loose information in the much weaker SV. The criteria should be revisited to improve, in order to choose a correct break iteration.

# Chapter 6

# Application of the method and Results

This chapter has the main goal of predicting the kind of results but also of difficulties we will find in modeling Mercury's magnetic field. I will work with the synthetic data, because, as we know, the measures of MESSENGER aren't available yet.

I will start to prepare the data, and after that I will process it using the computer program tested before.

## 6.1 Input parameters and data

### 6.1.1 Preparing synthetic measures

During its mission, the spacecraft will collect a huge amount of data. However, not all measurements are adequate to use in our calculations, and that's why it is required to select those measures that are important for us.

#### Calculation of MESSENGER orbits

A program called SPICE was used. SPICE is a software suite developed at NASA for making the geometric calculations needed to plan an interplanetary mission. SPICE is used by mission teams at NASA, ESA, JAXA, and other space agencies. Most versions of Celestia are built with the SPICE libraries, enabling Celestia to use navigational data direct from space missions. This software gives us the position of many bodies in the solar system (natural or artificial) in different coordinate systems [20].

Here, I use the program to calculate the orbits of the MESSENGER spacecraft,

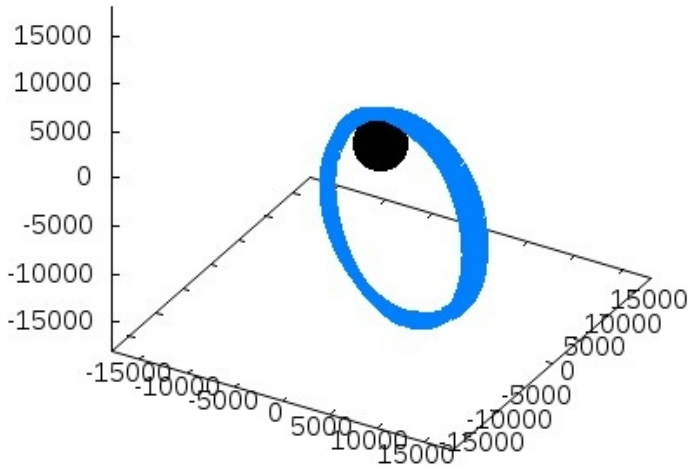


Figure 6.1: Orbit of MESSENGER spacecraft around Mercury, during 3 days of March 2012. X, Y and Z values are in km.

during the first year of mission, after the orbital insertion. They are calculated in cartesian coordinates, where the origin is the center of the planet (see figure 6.1).

During one year, the spacecraft covers all the planet's surface 6 times. Because of the satellite's eccentric orbit, the altitude has a very large variation between the north and south hemispheres, and consequently the measured intensity of the hermean magnetic field varies too.

### Selection of the data

There are two selections to do. One, to keep only the data that contain information relevant to the internal magnetic field of the planet, that means that I have to reject the data that is outside the magnetopause (see figure 6.2). The other, to select the data for which the signal is higher than the noise. These selections allow us to reduce the amount of data to use in the inverse problem.

### The magnetopause approximation

The reason I select the data that is inside the magnetopause (MP), is because I want to keep only the measures that have information on the magnetic field of Mercury originating inside the planet, not of the rest of the solar system (the interplanetary field). To do that, I used the Mercury paraboloid magnetospheric model [21]. This

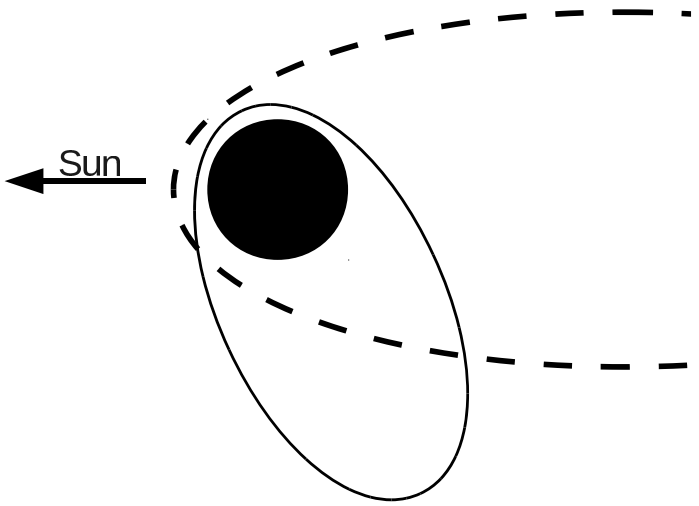


Figure 6.2: Scheme representative of the Mercury paraboloid magnetospheric model. The paraboloid is the dashed line, and the orbit of MESSENGER is in solid line.

model assumes that the magnetopause can be represented by a paraboloid of revolution along the planet-Sun direction, with equation 6.1,

$$2xR_1 = 2R_1^2 - y^2 - z^2 \tag{6.1}$$

where $R_1$ is the distance between the center of the planet and the subsolar point on the magnetopause. For Mercury, we have an average subsolar point distance of $R_1 = 1.4R_M$, where $R_M$ is Mercury's radius.

Figure 6.2 is a scheme that represents the paraboloid shape of the magnetopause and the orbit of the spacecraft around Mercury.

The selection consists in rejecting measures when the position of the MESSENGER satellite is outside the magnetopause. Figure 6.3 represents in red, the portion of the complete orbit that I keep for calculations.

**Data versus noise**

Before adding noise, I should select the maximal altitude where I have adequate measures to use in the calculations. The criteria to find this limit is that the root mean square value of the radial magnetic field be twice that of the noise magnitude

$$\langle B_r \rangle \simeq 2 \times \langle Noise \rangle \tag{6.2}$$

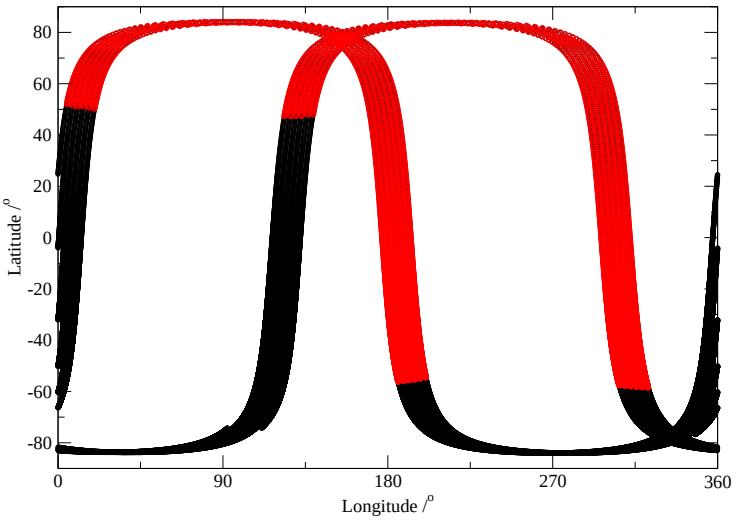


Figure 6.3: This figure shows the orbit of the spacecraft. The red color shows the portion of the orbit that is inside the magnetopause.

Assuming that the noise is 5 $nT$, I found the altitude of 3400 $km$. To find this altitude, I separated the data into spherical shells of thickness 100 $km$ and calculated the root mean square of the radial magnetic field in each shell.

The conclusion is that almost all measurements over the southern hemisphere are useless to characterize the internal magnetic field of internal origin.

### 6.1.2 Dipole grids

As I referred in section 5.1.1, I use the tesselation method called *polar coordinate subdivision*. It is this dipole distribution that gives the lower magnetic field over the sphere, when applied to the Runcorn's theorem conditions, where the ideal (theoretical) solution is a null magnetic field over the whole sphere. A singularity at the poles area subsists with the tesselation method that we use for the case of Mars [19], and figure 6.4 shows it. In one case, where we have data close to the north pole, we have to deal with a singularity point (at the north pole) that causes a perturbation in the estimated field, in the region around that point. The problem is solved by rotating the tesselation grid, in order to place the north pole at the equator, where the measurements are much higher in altitude, and less critical for the inversion.

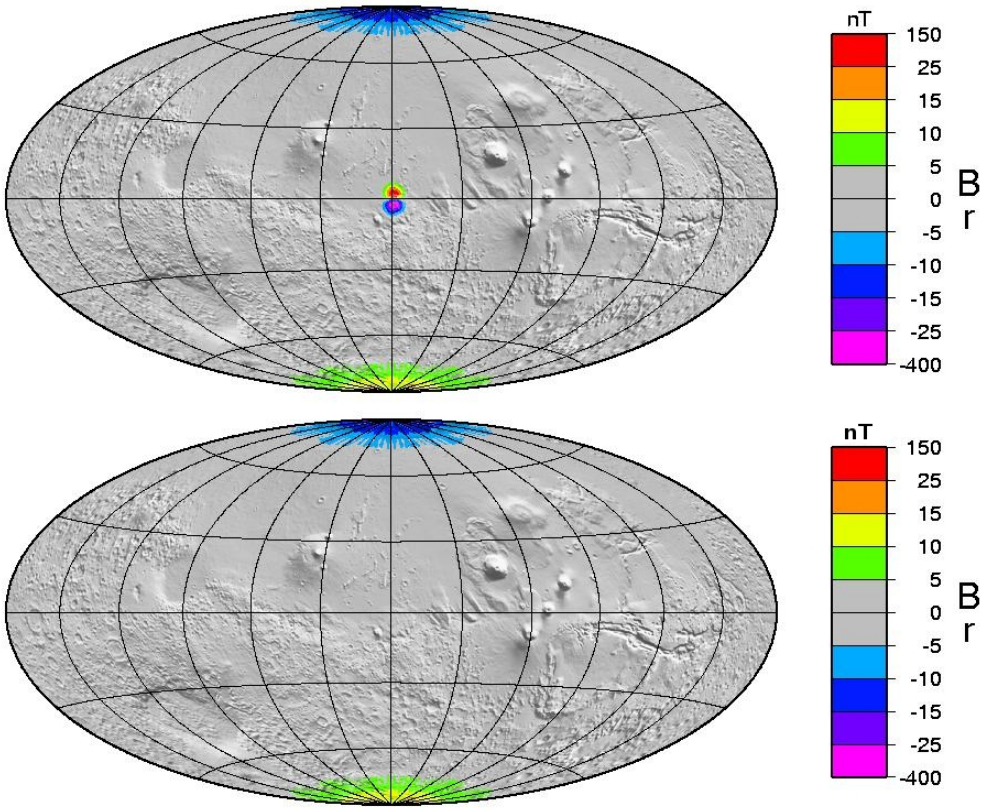


Figure 6.4: This figure shows the magnetic field that persists after the source has disappeared in tests done for Mars (Runcorn's theorem is applied) [19].

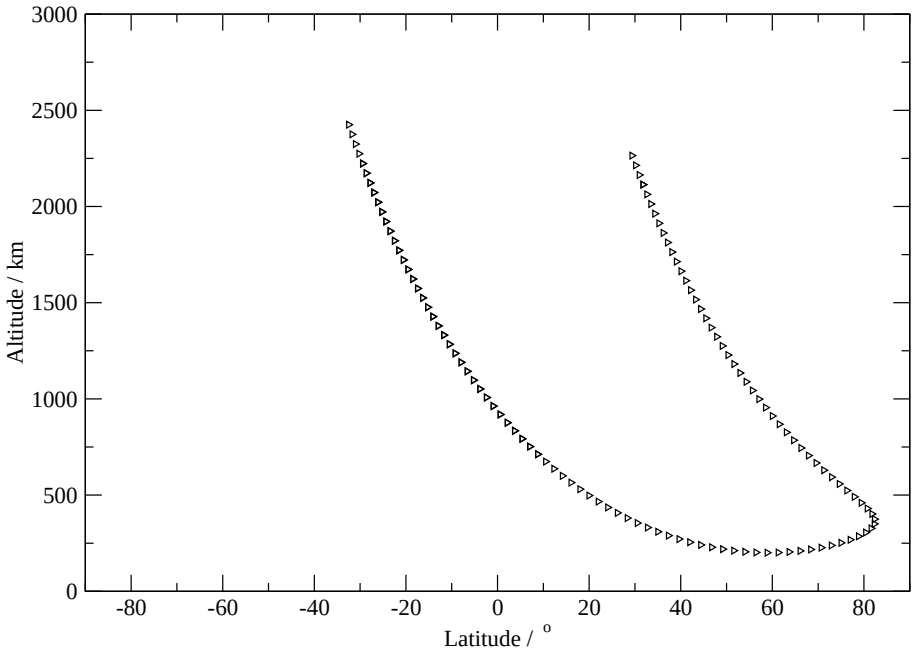


Figure 6.5: Altitude as a function of latitude, for selected positions of magnetic field measures, for only one orbit.

## 6.2 Discussion of results

After the inversion by the computer program, there are two options: 1) calculate the predicted magnetic field in a grid, and consequently loose the information of the orbit; and 2) do the direct calculation for the orbit positions. Both are necessary, the grid option is needed to represent maps, and the other is needed for the calculation of a true misfit, at the actual location of the observations.

I use the computer program to calculate the predicted magnetic field (the program was validated in chapter 5), from the measures that were selected in the previous section. Figure 6.5 shows the piece of the orbit of the spacecraft and which is kept after the selection criteria are applied. Analyzing all selected data, we have variation ranges for the altitude in the interval [200 $km$, 3400 $km$] from the surface of the planet, and for the latitude in the interval $[-44,5°, 84°]$.

For the following calculations, I will divide the dataset into two branches, to use

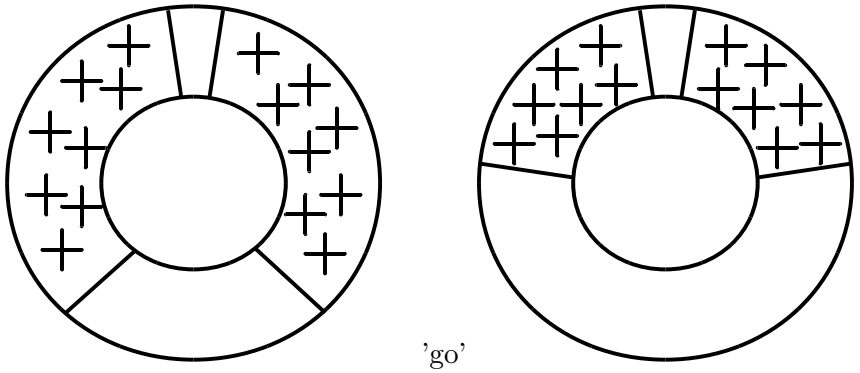


Figure 6.6: Schemes showing the distribution in latitude of observation values over Mercury (inside white circle), for the branches 'go' and 'back'.

as input data. I will denominate the lower branch as the "back branch", and the higher branch as the "go branch". The 'back' branch has a latitude range between $[-44, 5°, 84°]$, and the 'go' branch has a latitude range between $[14°, 83°]$. The altitude range is the same as for the of orbit. Figure 6.6 shows us the regions above the planet where we have magnetic field measures during the mission, for the 'back' and 'go' cases. As we can observe, there is a little hole centered in the north pole of diameter $\sim 10°$ and there is a lack of information over the south hemisphere, in both cases.

Before starting computations for an Hermean magnetic model, I should choose the minimal break iteration, to avoid spending useless computation time. For this, I calculate the misfit from equation 5.1. Figure 6.7 shows the misfit for the two branches, as a function of the iteration number. The 'go' branch shows a lower misfit than the other branch, and the reason is probably because the values of the radial magnetic field have a lower magnitude (higher altitudes). Applying the criteria defined by equation 5.4. I found a break iteration before the misfit stabilizes, due to oscillations on the curve. I tried using moving averages, that smooth the oscillations of the curve, but the used criteria still gives a too low break iteration. Finally, I chose the break iteration visually, and decided to leave for future work the choice of a better criteria.

In the following, I will use the magnetization model computed with a break iteration of 60.

One of the goals of this thesis is to find the latitude range where we can describe perfectly the magnetic field of the planet, using the time variable ESD method. To this end, it is necessary to define a misfit independent of the longitude. That is done by summing all the misfits with different longitudes, inside a latitude band (of 1°)

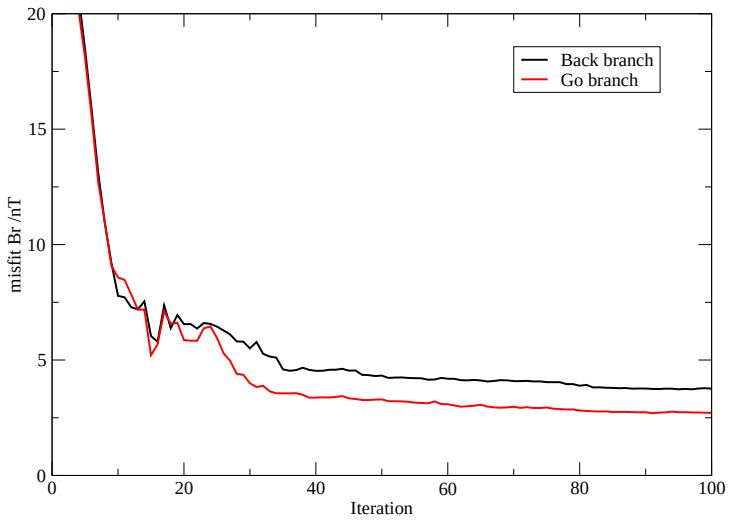


Figure 6.7: Misfit of the radial magnetic field component as function of the number of iterations, for the two branches.

and dividing by the number of summed values. We can visualize the problem as rings of misfits, above all the planet, and I call these "latitude band" misfits. The equation used for the misfit is equation 5.1.

Figure 6.8, shows the latitude band misfits for the 'go' and 'back' branches. For both cases, we see the misfit increases, from low to higher latitudes. We see also that the values are around 2 $nT$, probably because of the limited resolution of the implemented method, as referred in figure 5.4(b). Observing in detail the 'back' branch, we see lower band misfits in the south hemisphere probably due to the lower magnitude values of the magnetic field there (higher altitudes). The same effect can be seen in the 'go' branch, at latitudes around $20°N$. In the 'go' branch, for latitudes close to the north pole the misfit increases significantly. We could say that this is because of the hole of magnetic field information near the pole, but this idea is contradicted by the values of the 'back' branch, that don't show a similar behavior near the pole.

In the next three sections I calculate the predicted magnetic field: i) when the dipole distribution is rotated or not, to show if this procedure is required to eliminate any singularity at the north pole; ii) when the input data has or has not added noise,

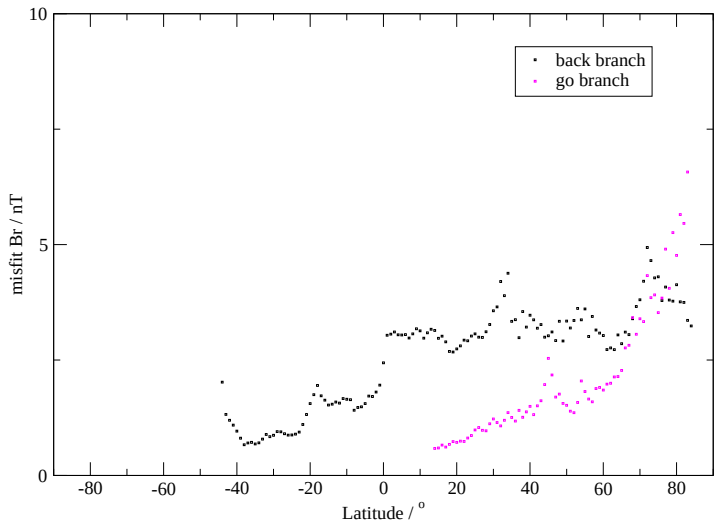


Figure 6.8: Latitude band misfit of the radial magnetic field component, as a function of latitude, for the two branches.

to show that the computer program can correctly model the magnetic field and not the noise; and finally, iii) for two input data grids at different times, to show that the secular variation of the magnetic field can be retrieved.

### 6.2.1 Rotation of the dipole grid

In this section, I calculate the predicted magnetic field, when I use two different input parameters for the dipole distribution. One has no rotation applied, and the other is rotated by 90°.

Figure 6.9 shows the misfit of the radial magnetic field component, when I apply the rotation to the dipole grid. Here we can see that when the rotation is applied, the 'back' branch attains to lower misfits.

Figure 6.10 shows the latitude band misfits, for the two branches 'go' and 'back', when the dipole distribution has or has not a rotation applied. From this figure we can't say that there are important differences when applying the rotation to the dipole grid. Probably, the reason is because in the north pole there is a measures-gap, that invalidates solving the singularity point problem by the rotation.

In order to visualize the differences between the predicted magnetic field and the

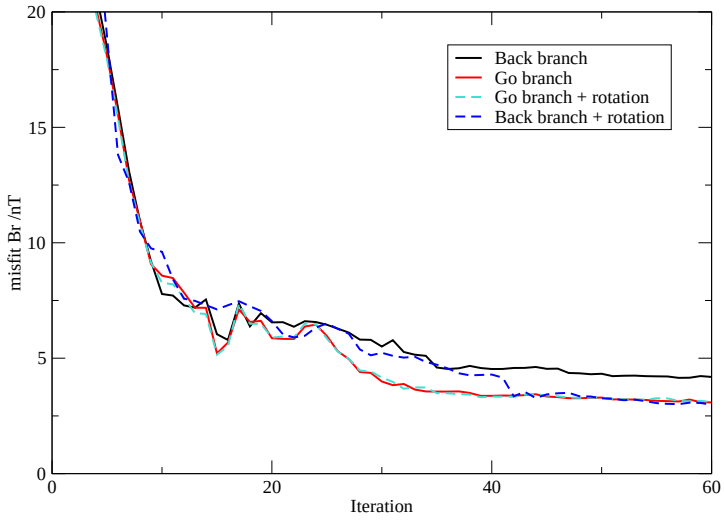


Figure 6.9: Misfit of the radial magnetic field component as a function of the number iterations, for the two branches, when the rotation of the dipoles grid is applied. The case without rotation is showed also, for comparison.

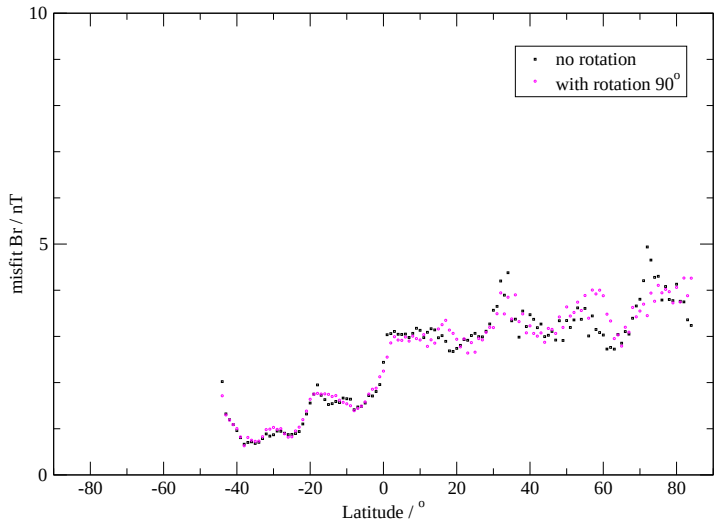


(a) 'Back' branch.

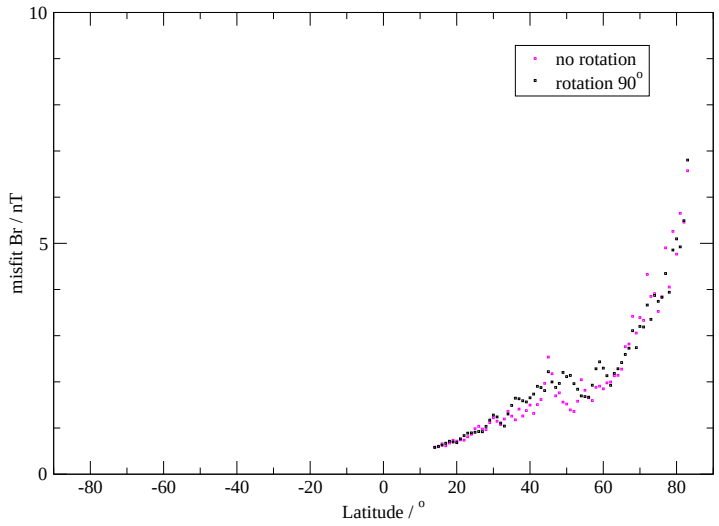


(b) 'Go' branch.

Figure 6.10: Latitude band misfit of the radial magnetic field component as a function of the latitude, when a rotation to the dipoles grid is applied. The band latitude misfits without rotation are also represented for comparison.

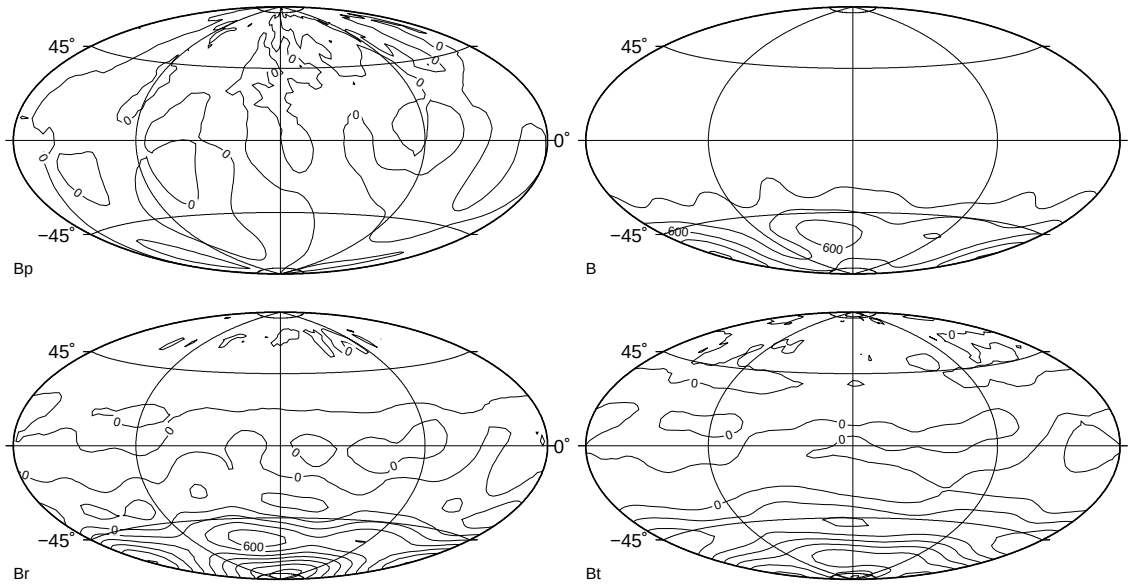


(a) 'Back' branch

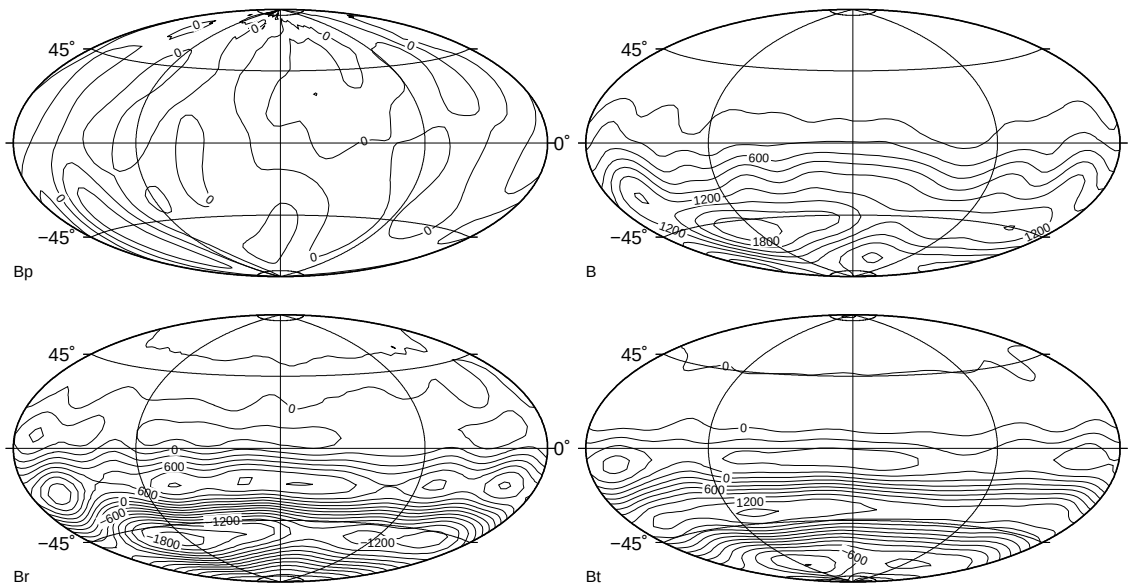


(b) 'Go' branch

Figure 6.11: Maps of the differences between the 'observed' and predicted magnetic fields, for the three magnetic field components ($B_r, B_\theta, B_\phi$), and for the total magnetic field, B, at 300 $km$ of altitude. Hammer projection is used, and the interval between contours is 200 $nT$.

observed one, represented in figure 4.7(a), I show maps of the differences between the observed and predicted magnetic fields.

Figure 6.11 shows the maps of the magnetic field differences, for the two branches. Considering the maps of the differences for the components $B_r$ and $B_\theta$ for the 'go' branch, we find very high values in the southern hemisphere, as expected since we don't have observations over that region. The errors are much lower over the southern hemisphere using the 'back' branch data. As for the total magnetic field differences we see that we obtain a good description of the observed measures down to lower latitudes in the 'back' branch. In summary, it is easily seen that the 'back' branch shows better results than the 'go' branch, because there are more measures for lower altitudes distributed over a larger range of latitudes.

In the next sections I will continue using the rotated dipole grid, because the misfit is lower for the 'back' branch when the rotation is applied (figure 6.9).

### 6.2.2 Noise perturbations

In this section, I calculate the predicted magnetic field for input data with white noise of amplitude 5 $nT$. The noise is represented in figure 6.12. As we can see from the map for the noise on the magnetic field amplitude, it is a white noise with zero mean.

Figure 6.13 shows the misfit of the radial magnetic field component, when I add noise to the input data. Here we can see that the misfit to the data with noise is larger. This is because the computer program can not fit a non potential field.

Figure 6.14 shows the latitude band misfit for the two branches. We see that, superposed to the resolution limit of the computer program (2 $nT$), there is the 5 $nT$ of noise added. That is explained because the computer program can not fit a non potential field (as the noise). The addition of noise attenuates the variations with latitude of the latitude band misfit, in both cases. Besides, for the 'go' branch, the increase of misfit values near the north pole isn't so marked as was without noise.

Figure 6.15 shows the differences between predicted magnetic field with noise and the ideal magnetic field, purely internal (without noise), for the three magnetic field components, and for the total magnetic field. Once more, when comparing the branches 'go' and 'back', it is the last one that shows the best results. Comparing this figure with figure 6.11, some perturbations for all the magnetic field components are noticed. Curiously, the latitude lower limit above which the main magnetic field is well explained by the model remains nearly the same with and without noise, both for the 'go' and the 'back' branches.

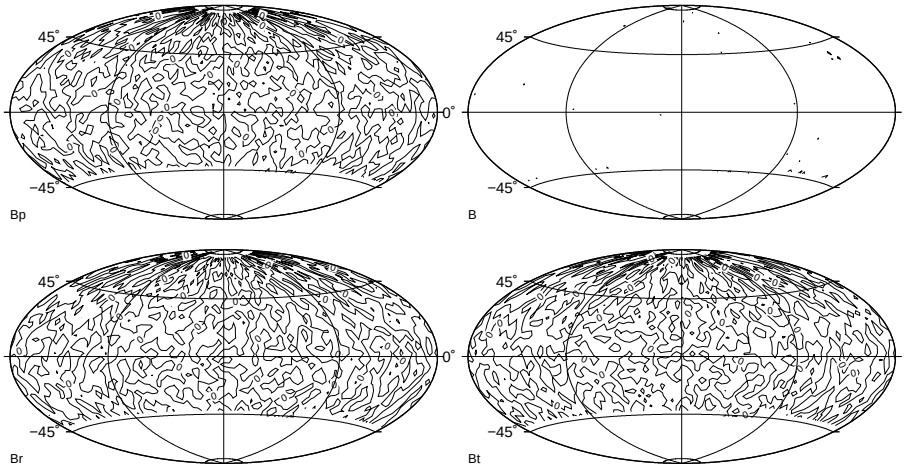


Figure 6.12: Maps of the noise added to the input 'data', for the three components $B_r, B_\theta, B_\phi$). Hammer projection is used.

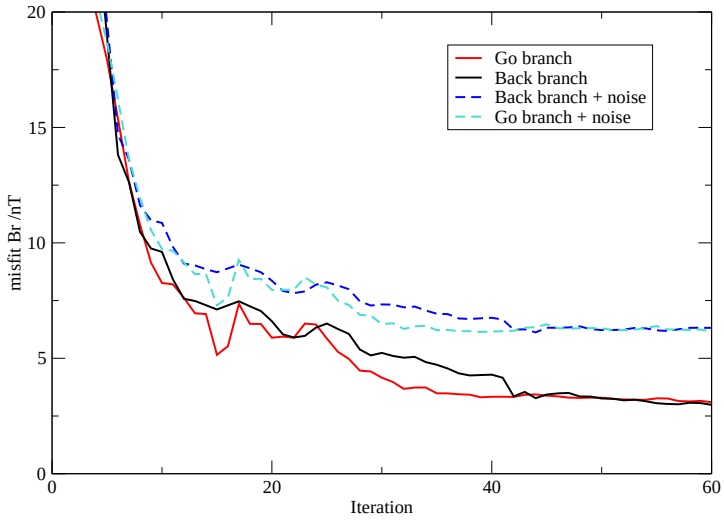


Figure 6.13: Misfit of the radial magnetic field component as a function of the number of iterations, for the two branches, when noise is added to the input data. The case without noise is showed also, for comparison.

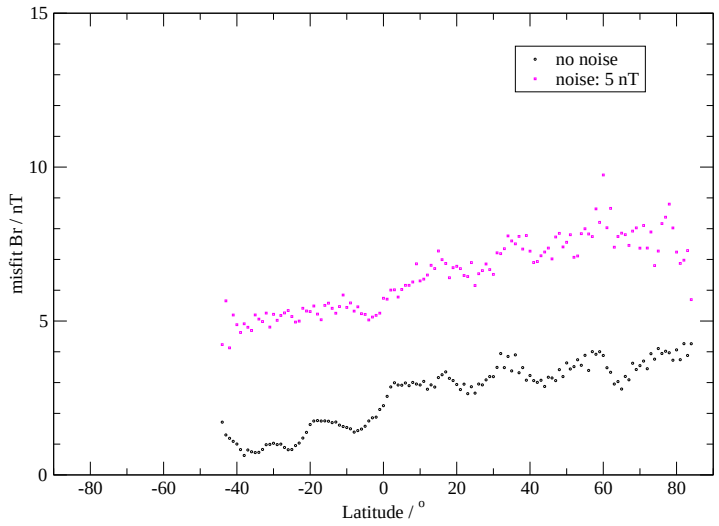


(a) Back branch

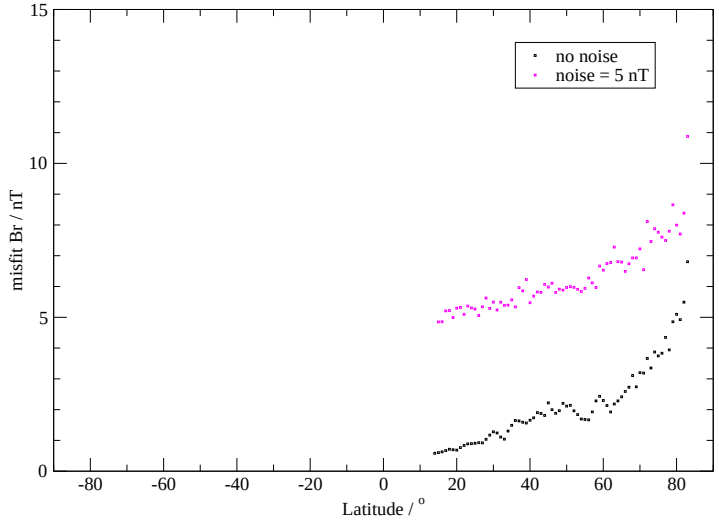


(b) Go branch

Figure 6.14: Latitude band misfit of the radial magnetic field component as a function of the latitude, when noise is added to the input data. The latitude band misfit without noise is also represented for comparison.

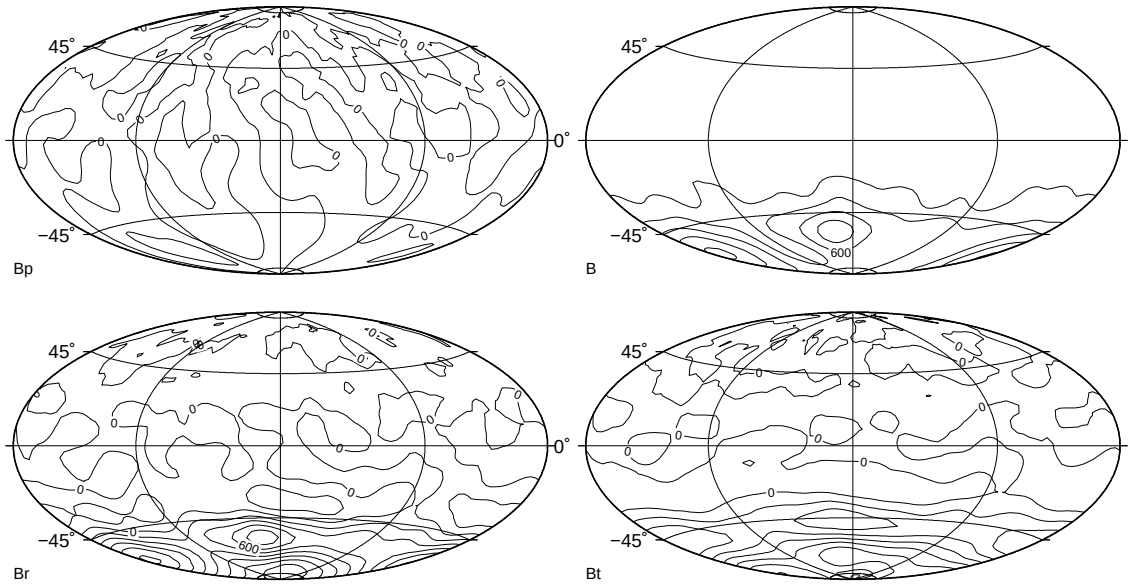


(a) 'Back' branch.

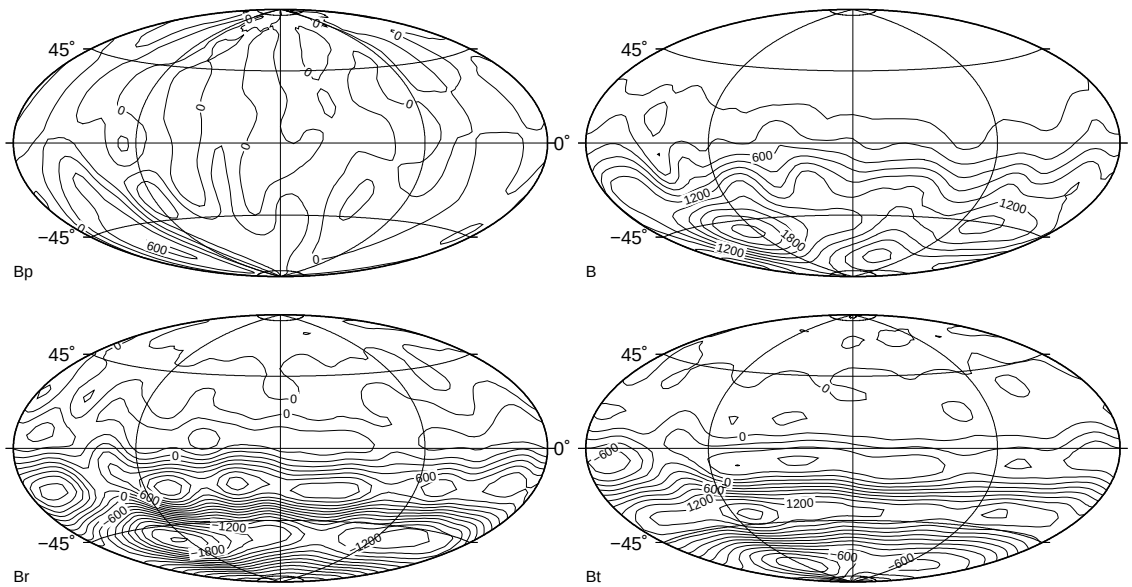


(b) 'Go' branch.

Figure 6.15: Maps of the differences between the theoretical magnetic field and the predicted magnetic field with noise, for the three magnetic field components $(B_r, B_\theta, B_\phi)$, and for the total magnetic field, B, at 300 $km$ altitude. Hammer projection is used, and the interval between contours is 200 $nT$.

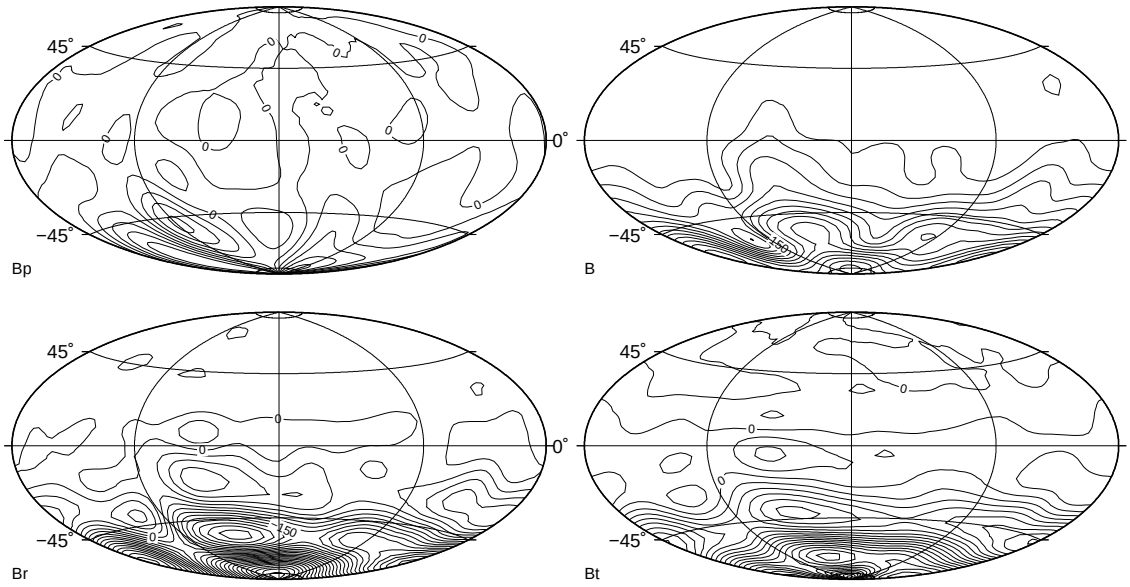


Figure 6.16: Maps of the difference between the observed and predicted secular variation (back branch), for the three components $(r, \theta, \phi)$, and for the secular variation, at 300 $km$ of altitude. Hammer projection is used, and each line to each line have a difference of 30 $nT$.

### 6.2.3 Secular Variation

To show that the secular variation is well resolved during the mission year, I calculate the differences between the secular variation predicted, and the input secular variation. Figure 6.16 shows these differences. We see that the lower limit of latitude above which the time varying ESD technique can model the secular variation, is higher than the lower latitude limit for the magnetic field. And it is this limit (close to the equator) that gives us the true latitude threshold to describe reasonably the planetary time-varying magnetic field, from our measures.

In chapter 5, I concluded that the inversion looses some information on the SV, when I invert $B(MF + SV)$. Here, we see that this loss of information is not so critical since it doesn't affect the modelisation of the SV for the North hemisphere.

# Chapter 7

# Conclusions and future work

This thesis work is like an iceberg, I just saw what is outside the water, but could perceive a lot more to uncover. Many new questions were raised at each step during this work, some of them I tried to answer, and many others I left for future work.

The main conclusion to retain here, is that the time dependent equivalent source dipoles technique works, for modeling Mercury's magnetic field and secular variation from a data set circumscribed to the North hemisphere, roughly. This method was developed here once the time-dependent spherical harmonic technique did not show good results for this specific problem, as shown in chapter 4.

When the new method was applied to our problem, in chapter 6, it was the secular variation that imposed a limit on latitude (around the equator), and this limit is the boundary of the region where we describe reasonably well the synthetic magnetic field and secular variation of the planet.

### Problems to solve

In chapter 5, the computer program I used to apply the new method was validated successfully, in spite of some reservations. In fact, the loss of a part of the secular variation information, during the inversion of $B(MF+SV)$ (main path), is a question that deserves reflection. If the true secular variation is still smaller than the one that I used here (Earth's secular variation divided by 10) the method will describe reasonably the data in a still smaller area, because the program will give less importance to the secular variation term.

Other question to solve is the choice of the right criteria to chose the break iteration. During my work, I achieved the conclusion that the criteria described by equation 5.4 doesn't work very well. This criteria was previously used in investiga-

tions of Mars crustal magnetic field, where the temporal variation is not present. The problem to solve for Mercury becomes more complex, and that's why the criteria needs to be more adjusted to the new situation.

One other test was done using the same criteria, to discover the core-mantle boundary (CMB) depth for Mercury. In fact, the size of Mercury's core is unknown to some hundreds of kilometers, and that's why it is required to test a method to find the CMB surface from the measured data collected by the spacecraft. The method used here consisted in placing the dipole grid distribution at different depths and using criteria 5.4 to each depth. The minimum value found, was expected to correspond to the true depth of the CMB. With the criteria from equation 5.4, the results were not good. I tried other criteria, and the best results that I got were obtained with the equation,

$$\frac{\sigma_{i-1} - \sigma_{i+1}}{\sigma_i} < 0.02 \tag{7.1}$$

as shown in figure 7.1.

As we can see, this produces an extended minimum region around the depth corresponding to the synthetic magnetic field measures. The flat region extends between $[340\ km, 740\ km]$, meaning that we can estimate to the true depth with an error of around $200\ km$.

Unfortunately, for the dipole parameter $n_d = 21$ this new criteria does not work.

**Waiting for the real data...**

In the end, it is with the real measures that we will find out how Mercury's dynamo works, if there is one.

With the new data, we will access the true latitude limit above which we can describe well the planetary magnetic field, because it depends on the secular variation magnitude. This secular variation carries important information on the sort of dynamo originating Mercury magnetic field. It is directly related to the liquid iron currents at the CMB, which can be computed from inversion of Mercury secular variation as done for Earth [22].

Finally, in the eventuality that it does not exist secular variation for Mercury, the method of ESD (without time variation) is expected to work properly, as it did for Mars.

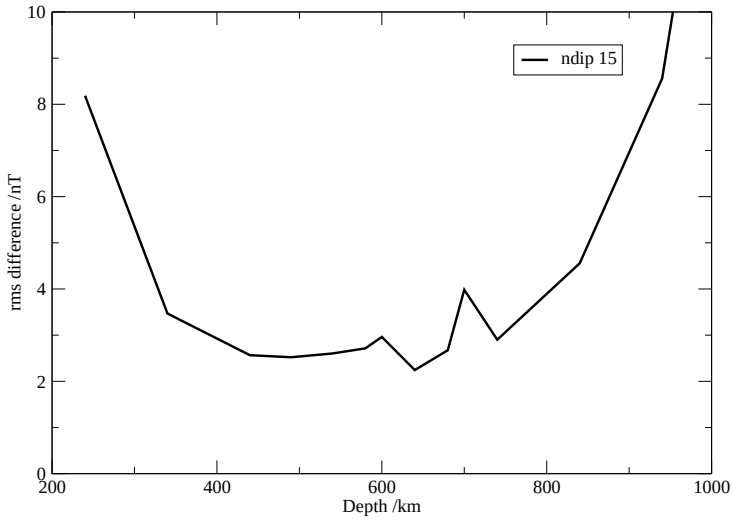


Figure 7.1: Misfit (or rms difference) as given by equation 7.1, as a function of depth, for a dipole parameter $n_d = 15$ and the CMB at a depth of 640 km.

# Appendix A

# Coefficient tables

Table A.1: Model using the first coefficient the real one, and the rest one's are the Earth's coefficients in Mercury's scale, with the CMB radius of 1800 km.

| n | m | g | h | $\dot{g}$ | $\dot{h}$ | n | m | g | h | $\dot{g}$ | $\dot{h}$ |
|---|---|---|---|---|---|---|---|---|---|---|---|
| 1 | 0 | -198000 | | 2.908 | | 6 | 0 | 2.159 | | 0.082 | |
| 1 | 1 | -11.267 | 34.158 | 3.157 | -5.386 | 6 | 1 | 2.040 | -0.584 | 0.191 | -0.487 |
| 2 | 0 | -20.923 | | -4.403 | | 6 | 2 | 2.246 | 1.663 | 0.327 | -1.984 |
| 2 | 1 | 27.478 | -23148 | -1.521 | -7.366 | 6 | 3 | -4.502 | 1.882 | 2.042 | -0.388 |
| 2 | 2 | 14.931 | -4.533 | -0.441 | -3.743 | 6 | 4 | -0.378 | -1.850 | -1.886 | -0.541 |
| 3 | 0 | 16.169 | | -0.014 | | 6 | 5 | 0.443 | 0.005 | -0.495 | 0.050 |
| 3 | 1 | -27.853 | -2.482 | -1.628 | 2.546 | 6 | 6 | -2.571 | 1.453 | 1.119 | 1.443 |
| 3 | 2 | 15.098 | 3.328 | -0.712 | -2.179 | 7 | 0 | 3.145 | | 0.168 | |
| 3 | 3 | 8.239 | -6.294 | -3.596 | -2.220 | 7 | 1 | -2.935 | -2.439 | -0.116 | 0.979 |
| 4 | 0 | 15.005 | | -1.274 | | 7 | 2 | -0.045 | -0.901 | -0.613 | 0.445 |
| 4 | 1 | 12.937 | 4.554 | 1.380 | 1.170 | 7 | 3 | 1.484 | 0.268 | 1.606 | 0.097 |
| 4 | 2 | 3.557 | -3.696 | -4.715 | 1.049 | 7 | 4 | 0.461 | 0.996 | 0.848 | 0.261 |
| 4 | 3 | -6.258 | 2.280 | 2.839 | 2.849 | 7 | 5 | 0.350 | 0.463 | 0.673 | -1.158 |
| 4 | 4 | 1.670 | -4.956 | -1.418 | -0.275 | 7 | 6 | 0.234 | -1.030 | -0.673 | -0.322 |
| 5 | 0 | -4.914 | | -1.291 | | 7 | 7 | 0.049 | -0.195 | 0.985 | 0.375 |
| 5 | 1 | 7.735 | 0.929 | 0.472 | -0.036 | 8 | 0 | 1.310 | | 0.029 | |
| 5 | 2 | 4.623 | 3.896 | -2.006 | 1.495 | 8 | 1 | 0.397 | 0.599 | 0.366 | -0.215 |
| 5 | 3 | -2.958 | -2.734 | -0.937 | 1.390 | 8 | 2 | -0.595 | -1.118 | -0.918 | 0.240 |
| 5 | 4 | -3.680 | -0.520 | 0.225 | 3.248 | 8 | 3 | -0.376 | 0.508 | 0.364 | 0.518 |
| 5 | 5 | -0.296 | 2.283 | 0.021 | -0.434 | 8 | 4 | -0.947 | -1.065 | -0.527 | 0.729 |

| n | m | g | h | $\dot{g}$ | $\dot{h}$ | n | m | g | h | $\dot{g}$ | $\dot{h}$ |
|---|---|---|---|---|---|---|---|---|---|---|---|
| 8 | 5 | 0.525 | 0.852 | 0.464 | 0.285 | 9 | 9 | -0.642 | 0.409 | -0.543 | 0.574 |
| 8 | 6 | 0.473 | 0.417 | 0.893 | -0.462 | 10 | 0 | -0.226 | | 0.229 | |
| 8 | 7 | -0.564 | -0.704 | -1.220 | 0.856 | 10 | 1 | -0.583 | 0.199 | -0.056 | 0.428 |
| 8 | 8 | -0.283 | -0.018 | 0.860 | 0.750 | 10 | 2 | 0.144 | 0.007 | -0.125 | -0.010 |
| 9 | 0 | 0.389 | | 0.168 | | 10 | 3 | -0.249 | 0.422 | 0.643 | 0.229 |
| 9 | 1 | 0.694 | -1.421 | 0.047 | -0.230 | 10 | 4 | -0.019 | 0.466 | 0.163 | -0.163 |
| 9 | 2 | 0.255 | 0.922 | 0.210 | -0.411 | 10 | 5 | 0.307 | -0.619 | -0.473 | -0.476 |
| 9 | 3 | -0.518 | 0.901 | 0.802 | 0.114 | 10 | 6 | 0.042 | -0.101 | -0.542 | 0.132 |
| 9 | 4 | 0.378 | -0.473 | -0.704 | -0.235 | 10 | 7 | 0.196 | -0.323 | 0.031 | -0.414 |
| 9 | 5 | -0.741 | -0.590 | -0.947 | 0.202 | 10 | 8 | 0.373 | -0.060 | -0.424 | -0.782 |
| 9 | 6 | -0.096 | 0.582 | 0.163 | -0.140 | 10 | 9 | 0.000 | -0.222 | -0.459 | -0.080 |
| 9 | 7 | 0.632 | 0.222 | -0.240 | -0.404 | 10 | 10 | -0.184 | -0.756 | -0.657 | -0.289 |
| 9 | 8 | -0.443 | -0.567 | -1.192 | 0.416 | | | | | | |

# Bibliography


[1] S. C. Solomon. Mercury: the enigmatic innermost planet. *Earth and Planetary Science Letters*, 216:441–455, December 2003.

[2] Dr. David R. Williams. NASA Goddard Space Flight Center. Mercury Fact Sheet, http://nssdc.gsfc.nasa.gov/planetary/factsheet/mercuryfact.html, November 2010.

[3] O. Verhoeven, P. Tarits, P. Vacher, A. Rivoldini, and T. van Hoolst. Composition and formation of Mercury: Constraints from future electrical conductivity measurements. *Planetary Space Science*, 57:296–305, March 2009.

[4] J. L. Margot, S. J. Peale, R. F. Jurgens, M. A. Slade, and I. V. Holin. Large Longitude Libration of Mercury Reveals a Molten Core. *Science*, 316:710–, May 2007.

[5] V. Malavergne, M. J. Toplis, S. Berthet, and J. Jones. Highly reducing conditions during core formation on Mercury: Implications for internal structure and the origin of a magnetic field. *Icarus*, 206:199–209, March 2010.

[6] N.F. Ness J.E.P. Connerney. *Mercury's magnetic field and interior, in: F. Vilas, C.R. Chapman, M.S. Matthews (Eds.), pp. 494513.* University of Arizona Press, Tucson, 1998.

[7] O. Aharonson, M. T. Zuber, and S. C. Solomon. Crustal remanence in an internally magnetized non-uniform shell: a possible source for Mercury's magnetic field? *Earth and Planetary Science Letters*, 218:261–268, February 2004.

[8] S. K. Runcorn. On the interpretation of lunar magnetism. *Physics of the Earth and Planetary Interiors*, 10:327–335, August 1975.

[9] B. J. Anderson, M. H. Acuña, H. Korth, M. E. Purucker, C. L. Johnson, J. A. Slavin, S. C. Solomon, and R. L. McNutt. The Structure of Mercury's Magnetic Field from MESSENGER's First Flyby. *Science*, 321:82–, July 2008.

[10] A. Balogh, R. Grard, S. C. Solomon, R. Schulz, Y. Langevin, Y. Kasaba, and M. Fujimoto. Missions to Mercury. *Space Science Reviews*, 132:611–645, October 2007.

[11] JHU/APL. MESSENGER, http://messenger.jhuapl.edu.

[12] B. Langlais, M. E. Purucker, and M. Mandea. Crustal magnetic field of Mars. *Journal of Geophysical Research (Planets)*, 109:E02008, February 2004.

[13] B. J. Anderson, M. H. Acuña, H. Korth, J. A. Slavin, H. Uno, C. L. Johnson, M. E. Purucker, S. C. Solomon, J. M. Raines, T. H. Zurbuchen, G. Gloeckler, and R. L. McNutt. The Magnetic Field of Mercury. *Space Science Reviews*, 152:307–339, May 2010.

[14] B. Langlais, M. Mandea, and P. Ultré-Guérard. High-resolution magnetic field modeling: application to MAGSAT and Ørsted data. *Physics of the Earth and Planetary Interiors*, 135:77–91, February 2003.

[15] S. Macmillan and R. Barraclough. An Evaluation of Candidate Geomagnetic Field Models for DGRF 1990 and IGRF 1995. *Geomagnetism and Geoelectricity*, 49:263–278, 1997.

[16] M. Purucker, D. Ravat, H. Frey, C. Voorhies, T. Sabaka, and M. Acuña. An altitude-normalized magnetic map of Mars and its interpretation. *Geophysics Research Letters*, 27:2449–2452, August 2000.

[17] J. Covington. Improvement of equivalent source inversion technique with a more symmetric dipole distribution model. *Physics of the Earth and Planetary Interiors*, 76:199–208, March 1993.

[18] Shahshahani M Katanforoush, A. Distributing Points on the Sphere. *Experimental Mathematics*, 12:199–209, 2003.

[19] M. Purucker. Annihilators at Mars: Are there alternative but reasonable magnetization distributions in the Martian crust that explain the MGS magnetic field obervations?. Poster at AGU (American Geophysical Union), 2004.

[20] NASA. SPICE, The NASA Planetary Science Division's Ancillary Information System, http://naif.jpl.nasa.gov/naif, Last Updated: 2 June 2011.

[21] I. Alexeev, E. Belenkaya, S. Bobrovnikov, J. Slavin, and M. Sarantos. A New Model of Mercury's magnetosphere. In *37th COSPAR Scientific Assembly*, volume 37, pages 57–+, 2008.

[22] M. A. Pais, O. Oliveira, and Nogueira F. Nonuniqueness of inverted core-mantle boundary flows and deviations from tagencial geostrophy. *Journal of Geophysical Research*, 109, 2004.